

## Appendix F–Finite Element Analysis of End Region

## Table of Contents

F.1	Modeling of End Region under Applied Loads .....	435
F.1.1	Model Configuration .....	435
F.1.2	Small Beam Model .....	440
F.1.3	Model Validation and Verification .....	442
F.1.4	Parametric Studies .....	446
F.1.5	Summary and Conclusions .....	463
F.2	Modeling of End Region during Prestress Transfer .....	466
F.2.1	Model Configuration .....	466
F.2.2	Model Validation and Verification .....	471
F.2.3	Transverse Force Quantification .....	476
F.2.4	Parametric Studies .....	478
F.2.5	Summary and Conclusions .....	497

## List of Figures

Figure 1–Coordinate system relative to load and supports .....	435
Figure 2–FE model configuration .....	436
Figure 3–Rigid shell and link elements.....	436
Figure 4–Bearing pad model.....	438
Figure 5–End region model dimensions .....	438
Figure 6–FE model symmetry .....	439
Figure 7–FE model top view.....	439
Figure 8–Comparison of small beam test setup, FE model details, and FE mesh .....	440
Figure 9–Bearing pad axial stiffness.....	442
Figure 10–Transverse strain (x-x) at end of beam for proposed and refined mesh .....	443
Figure 11–Small beam transverse (x-x) strain profile (V = 15 kip).....	443
Figure 12–Small beam load vs. deflection at load point.....	444
Figure 13–Small beam load vs. strain S5 (y-y).....	445
Figure 14–Small beam load vs. average of strain S11 and S12 (y-y).....	445
Figure 15–Maximum principal tensile (P1) strain location .....	446
Figure 16–Sensitivity study maximum transverse (x-x) strain .....	447
Figure 17–FIB and rectangular section FE models.....	448
Figure 18–Location of maximum flexural strain (normalizing strain) .....	450
Figure 19–Bursting behavior .....	450
Figure 20–Normalized transverse (x-x) strain at end of FIB-8.....	450
Figure 21–Flexural behavior.....	451
Figure 22–Normalized transverse (x-x) strain at end of FIB-16.....	451
Figure 23–Normalized transverse (x-x) strain vs. bearing pad width.....	453
Figure 24–Normalized transverse (x-x) strain vs. bearing pad width in FIB.....	454
Figure 25–Normalized transverse (x-x) strain vs. bearing pad width in rectangular section.....	455
Figure 26–Normalized transverse (x-x) strain vs. bearing pad width in small beam.....	456
Figure 27–Steel bearing plate beam and model .....	458
Figure 28–Bearing plate discretization .....	459
Figure 29–Effect of bearing plate and bearing pad width on transverse (x-x) strain.....	459
Figure 30–Normalized transverse (x-x) strain vs. bearing pad width in FIB section with steel bearing plate.....	460
Figure 31–Integration area for transverse force .....	462
Figure 32–Element x-x stress and y-z area .....	462
Figure 33–Net transverse (x-x) tensile force vs. bearing geometry .....	463
Figure 34–Coordinate system and free-body diagram of girder after prestress transfer.....	467
Figure 35–FE model details .....	468
Figure 36–Strand layout and element mesh.....	470
Figure 37–Verification study mesh densities.....	472
Figure 38–Verification study principal tensile stresses .....	472
Figure 39–Displaced shape .....	473
Figure 40–Comparison of experimental and FE model strains at cracks.....	474
Figure 41–Comparison of experimental and FE model transverse (x-x) strain .....	475
Figure 42–Comparison experimental and FE model longitudinal (y-y) strain .....	476
Figure 43–Comparison of experimental and FE model vertical (z-z) strain.....	476
Figure 44–Area over which stress was integrated to determine lateral force .....	477
Figure 45–Element x-x stress and y-z area .....	478
Figure 46–Transverse (x-x) stress at stages of prestress transfer.....	479

Figure 47–Variation in transverse force as strands are cut .....	480
Figure 48–Transverse (x-x) stress distribution at stage 1 (outer strands cut) with bearing plate and without bearing plate .....	482
Figure 49–Transverse (x-x) stress distribution at stage 2 (all strands cut) with bearing plate and without bearing plate .....	483
Figure 50–Transverse force vs. length of prestress transfer .....	484
Figure 51–Transverse stress distribution with 17.5-in. transfer length (50% of strands cut) .....	486
Figure 52–Transverse stress distribution with 42.5-in. transfer length (50% of strands cut) .....	487
Figure 53–Length of tension area vs. transfer length (50% of strands cut) .....	488
Figure 54–Transverse (x-x) stress at MID section through bottom flange (30% of strands cut).....	488
Figure 55–Flange splitting cracks at girder end.....	489
Figure 56–Lines for stress calculations.....	490
Figure 57–FE model stresses at girder end (50% strands cut) .....	490
Figure 58–Transverse (x-x) stress at mid-flange line (50% strands cut) .....	491
Figure 59–Average transverse (x-x) stress at end of girder due to strand cutting .....	491
Figure 60–AASHTO Type IV FEA model and analysis lines.....	493
Figure 61–Transverse stress distribution in Type IV girder (maximum condition) .....	494
Figure 62–Transverse (x-x) stress due to self-weight.....	495
Figure 63–Transverse (x-x) stress due to self-weight.....	496

## List of Tables

Table 1–Small beam FE model geometry .....	441
Table 2–Bearing stiffness sensitivity study details .....	447
Table 3–Model details: parametric study of bearing pad width.....	448
Table 4–Bearing pad properties .....	449
Table 5–Application of elastic loss.....	471
Table 6–Bearing plate study summary of transverse (x-x) stresses and forces .....	483
Table 7–Summary of transverse (x-x) stress at girder end due to strand cutting.....	492
Table 8–Summary of transverse (x-x) force at girder end due to strand cutting (FIB).....	492
Table 9–Summary of transverse (x-x) force at girder end due to strand cutting (Type IV) .....	493
Table 10–Transverse (x-x) stress due to self-weight .....	496

## 1 Modeling of End Region under Applied Loads

FE (finite element) modeling was conducted to 1) provide a better understanding of the elastic behavior of the end region prior to cracking and 2) to evaluate the effects of bearing pad stiffness and width on end region elastic stresses. The FEA (finite element analysis) program Adina (R&D 2009) was used to conduct all modeling and analysis. All models were linear elastic. Strain gage and displacement data from experimental work reported in Appendix B were used to validate the FEA model. Hereafter the beams reported in Appendix B are referred to as the “small beams.”

### 1.1 Model Configuration

The FE model was configured to be computationally efficient, yet able to capture the overall behavior of the beam as well as the local behavior of the end region. The ability of the model to capture the distribution of transverse tensile strain in the end region was of particular interest. The model was also designed such that the geometric and material properties could be adjusted to evaluate the sensitivity of the end region behavior to such parameters.

The coordinate system defined in Appendix D was also used in the FE models (Figure 1). The origin was located at the end of the beam nearest the point load, at the centerline of the cross-section, and at the bottom of the beam. The X axis was oriented horizontally across the cross-section, the Y axis was oriented horizontally along the length of the beam, and the Z axis was oriented vertically.

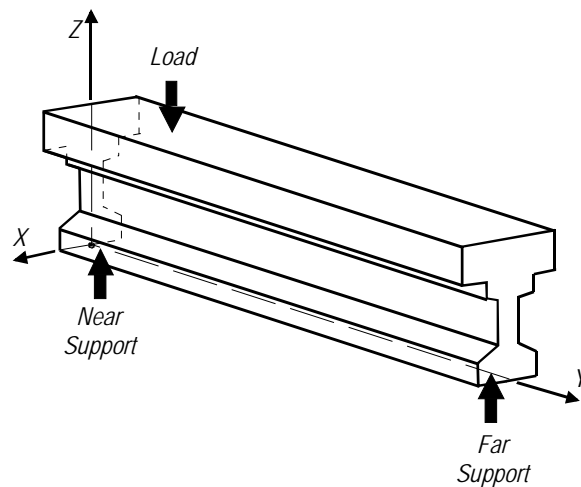


Figure 1—Coordinate system relative to load and supports

Figure 2 shows the model configuration. The shear span (distance from the load to the near support) and a small distance beyond the shear span were modeled with 27-node 3D solid elements on a primarily rectangular mesh. The remainder of the beam was modeled with 1D beam elements, with the transition from beam to solid elements made using rigid 2D shell elements and 1D rigid links. Rigid shell and link elements (Figure 3) coupled the displacements of the 3D solid elements with the displacements and rotations of the 1D beam elements. Transitioning to beam elements reduced the computational demand of the model while still modeling the global beam behavior and boundary conditions. Beam elements were placed at the centroid of the cross-section and were assigned cross-sectional properties equivalent to the physical beam. At the far support, a rigid link was provided to connect the beam elements to the physical location of the bearing pad at the bottom of the beam.

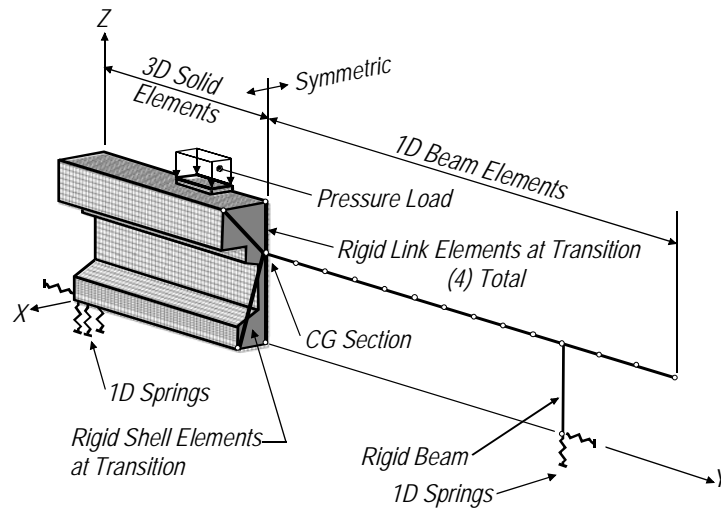


Figure 2–FE model configuration

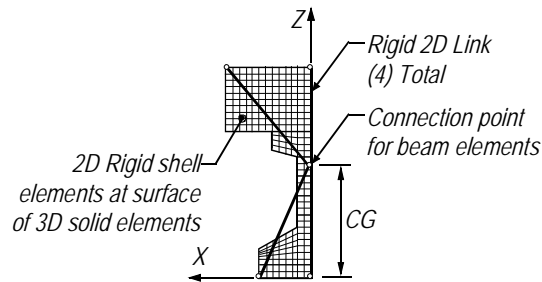


Figure 3–Rigid shell and link elements

Axial and shear stiffness of the bearing pad at the far support were modeled with 1D springs in the Z and Y directions respectively. At the near support, the axial and shear stiffness of the bearing pad was modeled with multiple spring elements in each of the X, Y, and Z directions. Position and quantity of spring elements matched the discretization of the solid elements used to model the beam (Figure 4). Stiffness was assigned to each spring in proportion to the tributary area represented by the spring.

Figure 5 defines key geometric variables of the model end region. Geometric variables were setup to allow variation of features such as shear span-to-depth ratio, bearing pad size and location, span length, and the location of the applied load. Additional geometric variables were defined on the cross section shown in Figure 6.

The cross-section, boundary conditions and load were symmetrical about the Y-Z plane, allowing for only half of the beam to be considered in the FE model (Figure 6). A top view of the model, shown in Figure 7, gives the position of the model relative to the physical geometry of the beam.

Concrete modulus of elasticity used for each model was 5300ksi, and the Poisson's ratio was defined as 0.2. The modulus of elasticity value was chosen to match the tested material properties from the physical beams used for model validation.

The typical model configuration described above was validated by comparison with experimental data, and was then used in more general investigations of the stress and strain state in the end region. Details of the validation and general investigations are contained in the proceeding sections.

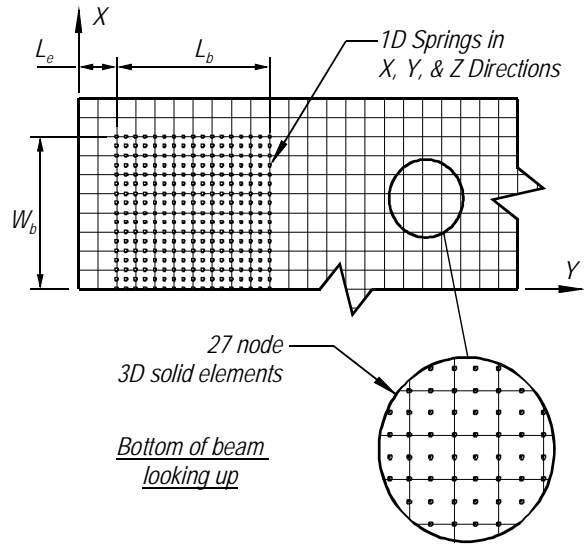


Figure 4–Bearing pad model

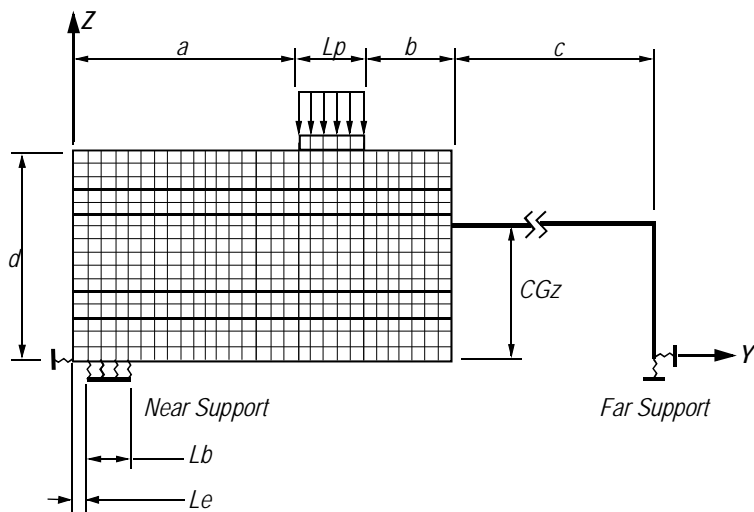


Figure 5–End region model dimensions

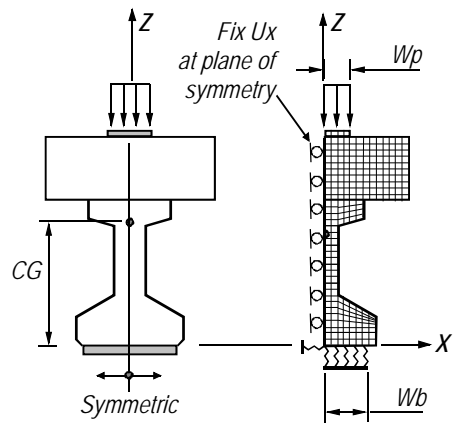


Figure 6–FE model symmetry

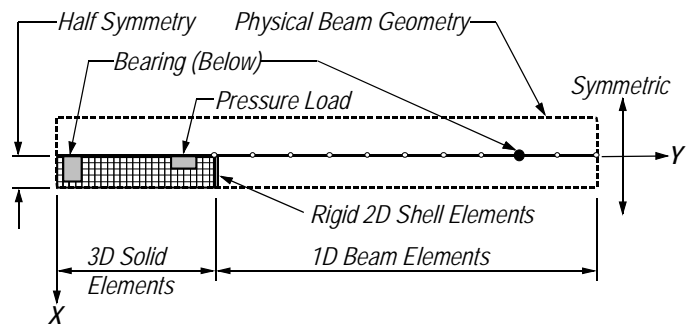


Figure 7–FE model top view

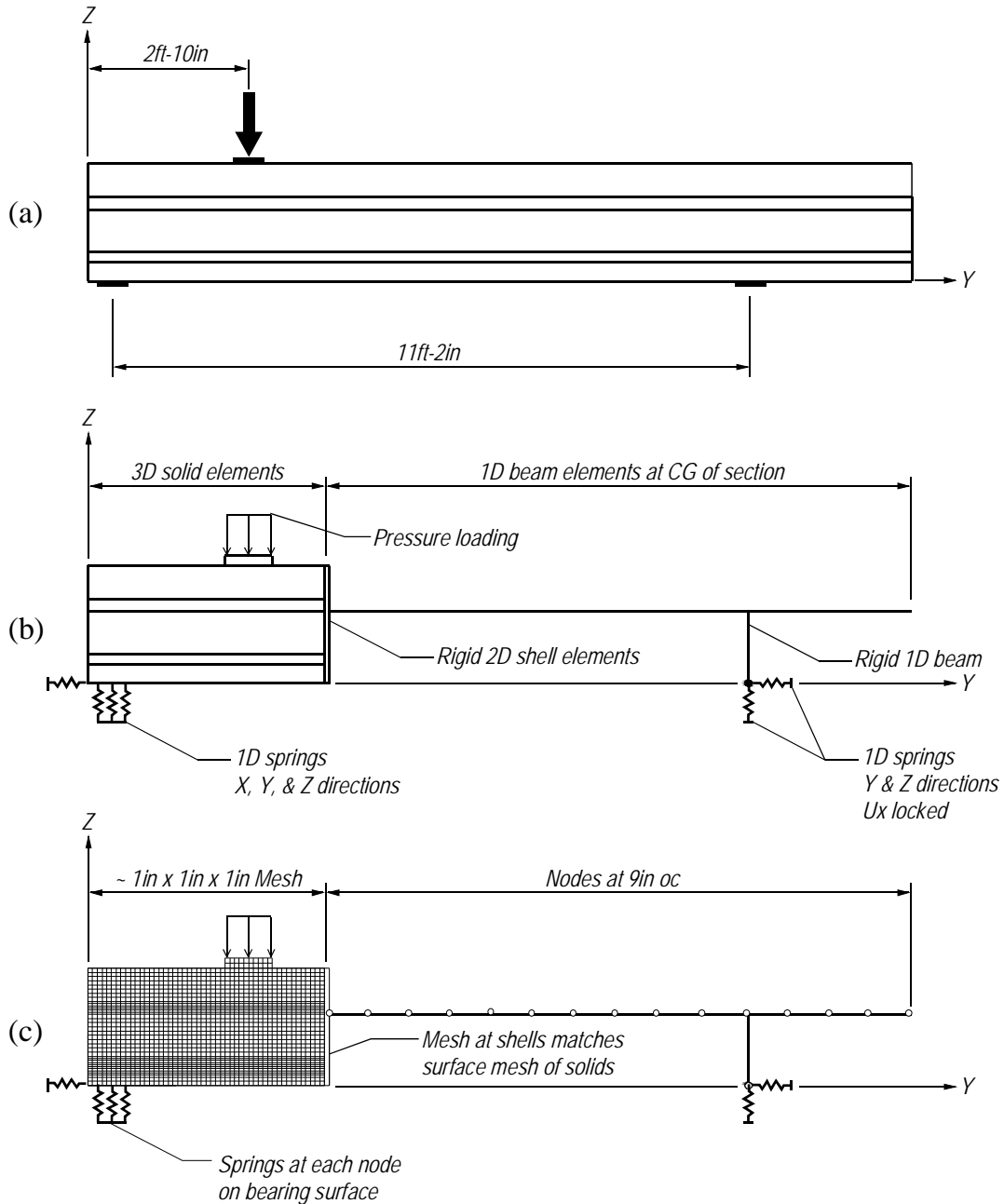


Figure 8—Comparison of small beam test setup, FE model details, and FE mesh

## 1.2 Small Beam Model

The configuration described above was used to model the small beam tests reported in Appendix B. Dimensions, element sizes, and spring properties of the model are listed in Table 1. Variables in this table are defined in Figure 5 and Figure 6. The experimental test setup being modeled, element types, and element density are shown in Figure 8. Stiffness values for the

springs in the Z direction were based on experimental load-displacement data from LVDTs located over the bearing pads on the small beam tests (Figure 9). From these data, a representative axial stiffness of 1150 kip/in was chosen. At the far support, the full axial stiffness was assigned to the single spring at the bearing point. At the near support the axial stiffness was distributed to the springs based in proportion to tributary area. Stiffness of springs at both the near and far supports in the pad shear directions (X & Y) were based on properties reported for similar sized bearing pads (Yura et al. 2001).

Table 1–Small beam FE model geometry

Dimension/Property	Value
A	29 in
B	11 in
C	90 in
D	28 in
CGz	17 in
Lp	10 in
Wp	5 in
Lb	7 in
Wb	6.5 in
Le	2 in
Near support Ka	8 kip/in
Near support Kv	0.05 kip/in
Far support Ka	1150 kip/in
Far support Kv	10 kip/in
3D solid element size	Approximately rectangular 1 in x 1 in x1 in
2D shell element size	Approximately square 1 in x 1 in
1D beam element size	9 in

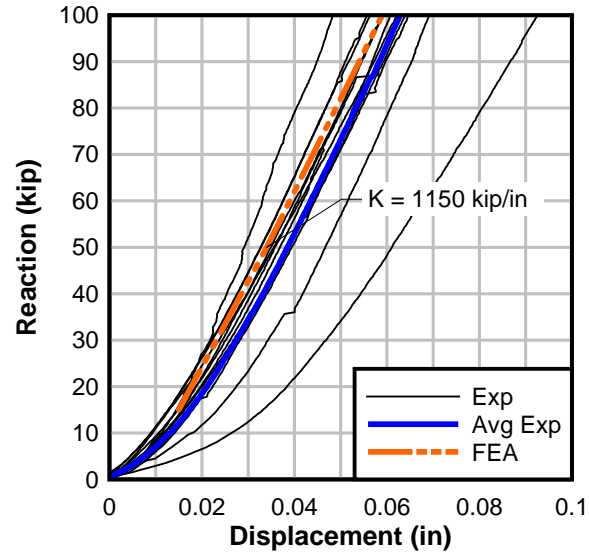


Figure 9–Bearing pad axial stiffness

### 1.3 Model Validation and Verification

Prior to comparing FE results with experimental data, convergence of the FE solution was verified by comparing the proposed model with a model containing a more refined mesh. Figure 10 shows the transverse (x-x) strain in the bottom bulb at the near support for the proposed and refined mesh densities. Note that the section geometry and strain values were symmetric about the Y-Z plane, and that only half of the bottom bulb is shown in the figure. The strain values and strain distributions were similar for both models, with the maximum transverse strain occurring at the centerline of the beam directly above the bearing pad ( $Z=0, X=0$ ). The refined model reported a maximum strain that was only 0.1% greater than the maximum value from the proposed model. Based on the degree of correlation with the refined mesh, element sizes used in the proposed model were considered appropriate.

Comparison with experimental data indicated that the FE model did an adequate job of capturing both the global and local linear elastic behavior of the physical test beams. Global behavior is compared in the load-displacement plot in Figure 12. Displacement in the figure (both experimental and analytical) was the vertical displacement at the load point, which was corrected to remove displacement due to deformation of the bearing pads. Within the elastic range, the FE model stiffness was 23% less stiff than the average experimental beam stiffness, but was still within the scatter of the experimental data.

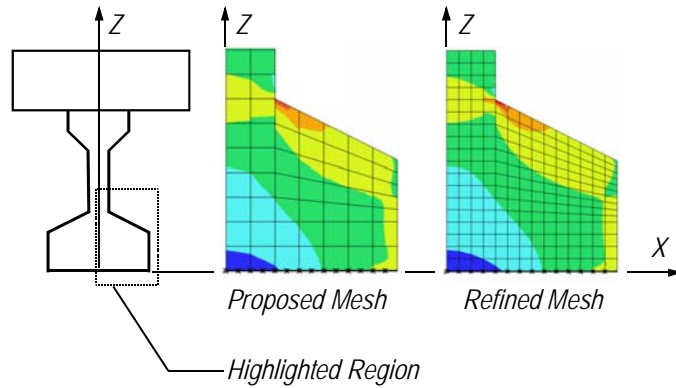


Figure 10–Transverse strain (x-x) at end of beam for proposed and refined mesh

The profile of the transverse (x-x) strain at the near end of the beam is shown in Figure 11. Strain profiles were compared at a load of 15 kip, as this load was well within the elastic range for each of the test beams. Experimental data came from strain gages mounted at the end of the beams 5 in. above the beam bottom. Shape of the strain profile was consistent between experimental data and the FE model, with the peak occurring at the centerline of the beam. Strain values calculated by the FE model were larger than the average of the experimental data, but were still within the scatter of the data.

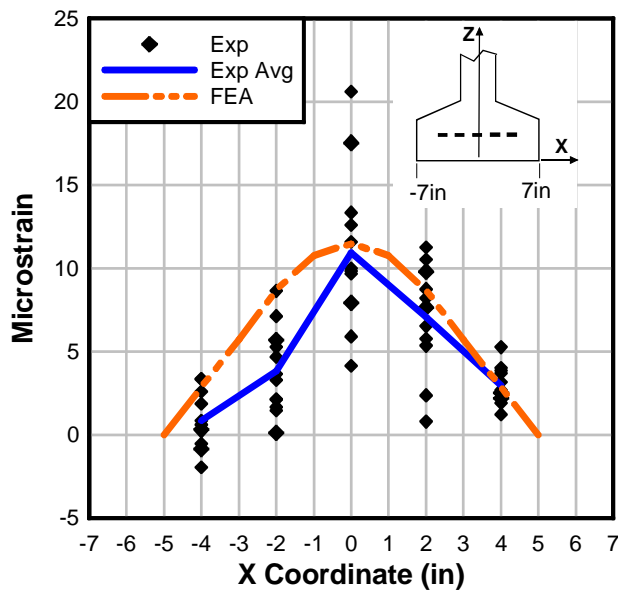


Figure 11–Small beam transverse (x-x) strain profile (V = 15 kip)

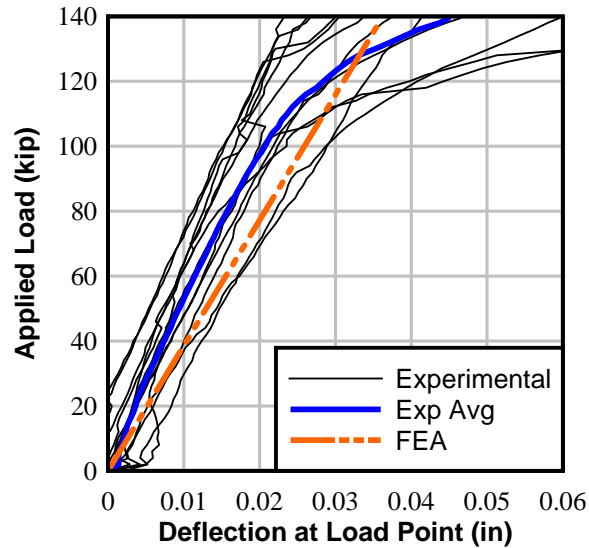


Figure 12–Small beam load vs. deflection at load point

Figure 13 shows the load versus strain relationship for gage S5, which was oriented longitudinally on the bottom of the beam directly below the applied load. Experimental data from gage S5 was consistent between tests. At the location of S5, the slope of the load-strain curve from the FE model was 20% less than the average slope of the experimental data.

Figure 14 shows the load versus strain relationship for gages S11 and S12. These gages were located on the top of the beam on either side of the applied load. Values from gages S11 and S12 were averaged to form the curves for the individual tests. Values reported by the FE model at the locations of S11 and S12 were identical because the FE model employed symmetry about the Y-Z plane. The slope of the load-strain curve reported by FE model was 5% greater than the average slope of the experimental data.

Finally, the maximum principal tensile strain was compared over the region shown in Figure 15. The maximum principle tensile strain occurred at the intersection of the web and the bottom bulb (Figure 15). The strain concentration at the web-bulb interface correlates with the location of cracks observed during testing.

The proposed FE model captured the general behavior of the physical beam, as well as the local behavior of the end region. In most cases, the FE results were within the scatter of the experimental data. Based on the correlations presented above, the proposed FE model was considered adequate for conducting more general evaluations of the concrete girder end region.

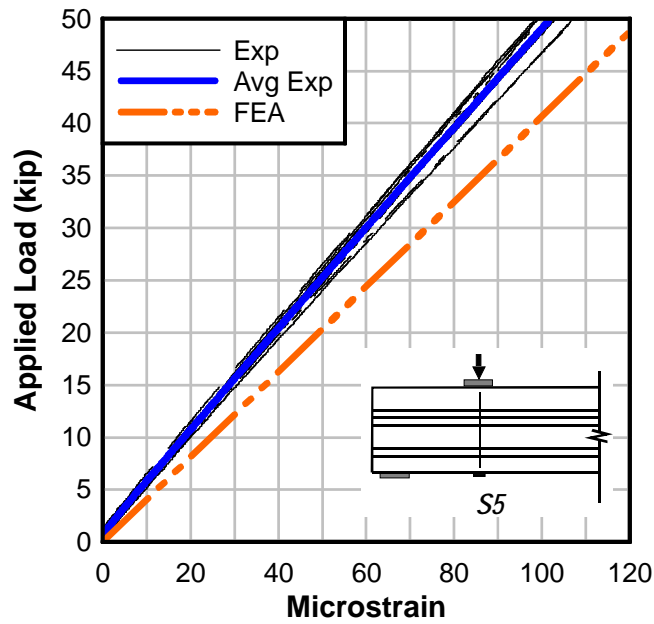


Figure 13–Small beam load vs. strain S5 (y-y)

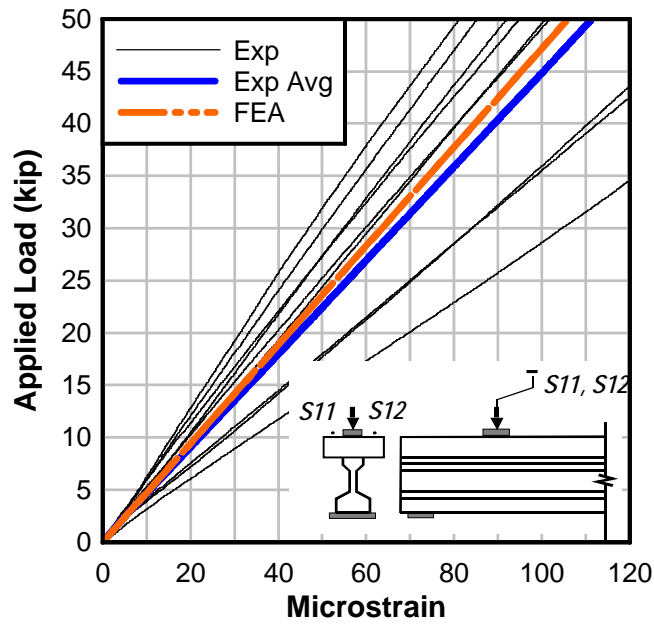


Figure 14–Small beam load vs. average of strain S11 and S12 (y-y)

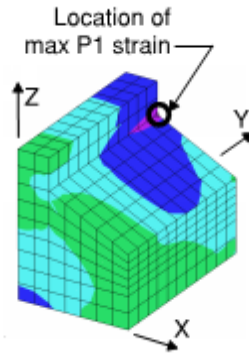


Figure 15–Maximum principal tensile (P1) strain location

#### 1.4 Parametric Studies

The FE model configuration presented previously was used to evaluate parameters affecting the strain state in the end region including bearing pad stiffness, cross-section geometry, steel bearing plates, and bearing pad geometry.

##### 1.4.1 Bearing Pad Stiffness

Four additional models were created to evaluate sensitivity of the end region strains to changes in bearing pad stiffness. In these models, the axial or shear stiffness of the bearing pad was either doubled or halved relative to the stiffness of the original model. By using half or double the stiffness properties of the original small beam model, the additional models cover the range of stiffness values for similar sized bearing pads reported by Yura et al. (2001). Details and results from the additional models are presented in Table 2. Information regarding the original model is also included in the table for reference.

Strain results were evaluated over the region shown in Figure 16. For each model, the maximum transverse tensile strain was located at the centerline of the beam directly above the bearing pad (Figure 16). Changes to bearing pad shear stiffness ( $K_v$ ) had negligible effect on maximum transverse (x-x) strain over the range of values tested. However, changes to the axial stiffness ( $K_a$ ) of the bearing pads did affect the maximum transverse strain. For the region considered, doubling the axial stiffness resulted in a 2.7% reduction in maximum transverse strain whereas halving the axial stiffness resulted in a 1.5% increase in maximum transverse strain.

Table 2–Bearing stiffness sensitivity study details

Model ID	Axial stiffness (kip/in)	Shear stiffness (kip/in)	Max tensile transverse strain ( $\epsilon_x$ ) for V = 15 kip (microstrain)	Change in max tensile transverse strain
Original	1150	10	26.64	--
x1/2 Axial stiffness	575	10	27.03	+1.5%
x2 Axial stiffness	2300	10	25.91	-2.7%
x1/2 Shear stiffness	1150	5	26.67	+0.1%
x2 Shear stiffness	1150	20	26.61	-0.1%

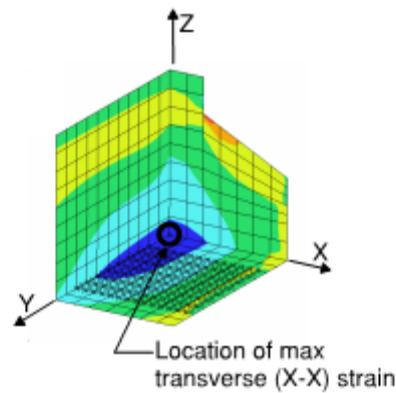


Figure 16–Sensitivity study maximum transverse (x-x) strain

#### 1.4.2 Bearing Pad Geometry

To evaluate the effect of bearing pad width on the transverse strain in the end region, FE models of the Florida I-Beam (FIB) and a rectangular cross-section (Figure 17) were created using the modeling configuration described previously. Details of the models are given in Table 3. The bearing pad width,  $W_b$ , was varied from 8.55 in. to 16.15 in. Because half-symmetry models were used, the bearing pad width,  $W_b$ , was equal to half of the total bearing pad width. Thus the FE model with  $W_b$  of 16.15 in. corresponded to a total bearing pad width of 32.3 in. This dimension is similar to the 32 in. width specified in the FDOT design standards (FDOT 2009).

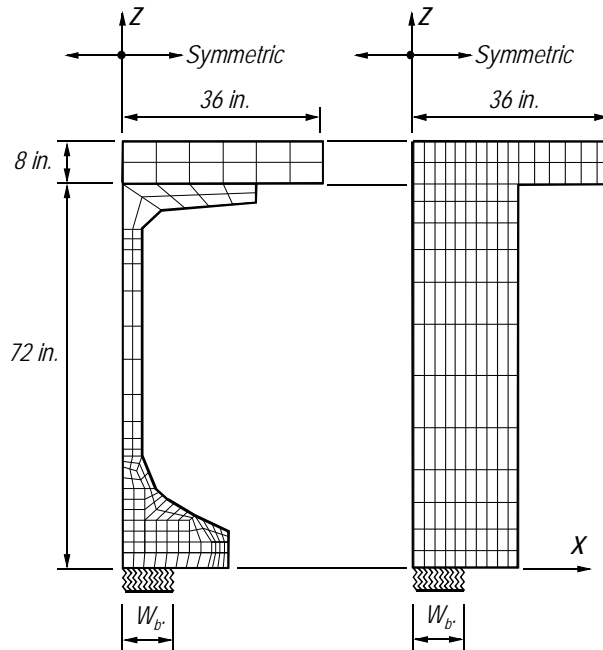


Figure 17–FIB and rectangular section FE models

Table 3–Model details: parametric study of bearing pad width

a	120 in
b	32 in
c	1032 in
d	80 in
CGZ	47.7 in
Lp	16 in
Wp	6 in
Lb	10 in
Wb	Varies

For convenience, models were assigned a label based on cross-section shape and nominal  $W_b$  dimension. For example, the label FIB-10 was assigned to the model with the FIB cross-section and a bearing pad width of 10.45 in. The label R-15 was given to the model with the rectangular cross-section and a bearing with of 15.20 in.

Stiffness and spacing of the individual springs comprising the bearing pad at the near support were held constant even as the bearing pad width varied. However, the total stiffness of the bearing pad changed as additional springs were added or removed to change the width of the bearing pad. Individual spring stiffness and total bearing pad stiffness are listed in Table 4. In each model, total the stiffness of the far support matched the stiffness of the near support.

Table 4–Bearing pad properties

	Half Symmetry			Total	
	Wb	Ka	Kv	Ka	Kv
FIB-8, R-8	8.55 in.	2710 kip/in.	5.4 kip/in.	5420 kip/in.	10.8 kip/in.
FIB-9, R-9	9.50 in.	2995 kip/in.	6.0 kip/in.	5990 kip/in.	12.0 kip/in.
FIB-10, R-10	10.45 in.	3280 kip/in.	6.6 kip/in.	6560 kip/in.	13.2 kip/in.
FIB-11, R-11	11.40 in.	3565 kip/in.	7.2 kip/in.	7130 kip/in.	14.4 kip/in.
FIB-12, R-12	12.35 in.	3850 kip/in.	7.7 kip/in.	7700 kip/in.	15.4 kip/in.
FIB-13, R-13	13.30 in.	4135 kip/in.	8.3 kip/in.	8270 kip/in.	16.6 kip/in.
FIB-14, R-14	14.25 in.	4420 kip/in.	8.9 kip/in.	8840 kip/in.	17.8 kip/in.
FIB-15, R-15	15.20 in.	4710 kip/in.	9.4 kip/in.	9420 kip/in.	18.8 kip/in.
FIB-16, R-16	16.15 in.	4995 kip/in.	10.0 kip/in.	9990 kip/in.	20.0 kip/in.
Axial stiffness of individual springs at near support = 31.7 kip/in.					
Shear stiffness of individual springs at near support = 0.0635 kip/in.					

Transverse (x-x) strain results from the models were normalized by the maximum flexural ( $\epsilon_{y,max}$ ) tensile strain from the FIB model. The maximum flexural strain was located at the bottom of the beam below the load point (Figure 18). The value of  $\epsilon_{y,max}$  was slightly different for the FIB and rectangular cross-sections; for a given section, however, it did not vary as the bearing pad width changed. For a half-symmetry applied load of 67 kip (experimental load of 134 kip),  $\epsilon_{y,max}$  was 91 microstrain for the FIB model, and for the same load was 61 microstrain for the rectangular section model. The transverse strains for each model were normalized by  $\epsilon_{y,max}$  from the FIB model.

For the FIB cross-section, two types of behavior were observed as the bearing pad width was adjusted. First, when the pad width was narrow, the transverse strains were distributed in a bottle shape between the bearing pad and the bottom of the web (Figure 19). This was denoted as ‘bursting’ behavior. The mechanics of bursting behavior are similar to a split cylinder test, with transfer tensile strain forming perpendicular to compressive loads. The maximum transverse strain occurred above the bearing pad, as shown in Figure 20. As the pad width increased, flexural strains increased at the bottom edge of the flange as the load spread to the far edge of the bearing pad (Figure 21). This is denoted as ‘flexural’ behavior. For ‘flexural’ behavior, the maximum transverse strain occurred at the bottom of the section as shown in Figure 22.

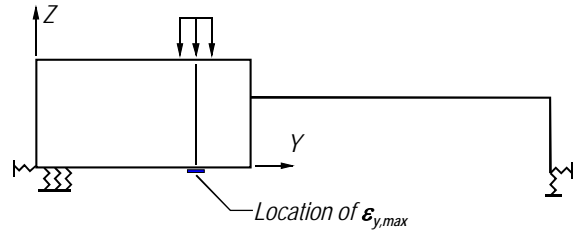


Figure 18–Location of maximum flexural strain (normalizing strain)

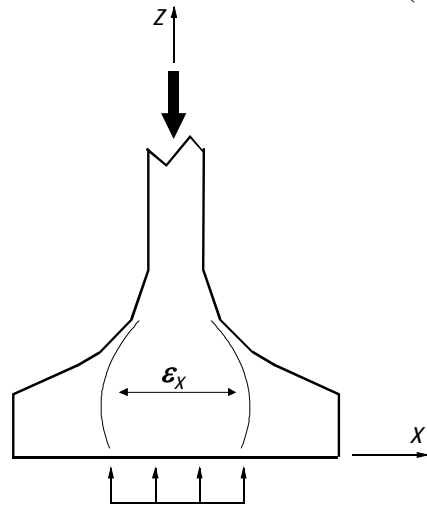


Figure 19–Bursting behavior

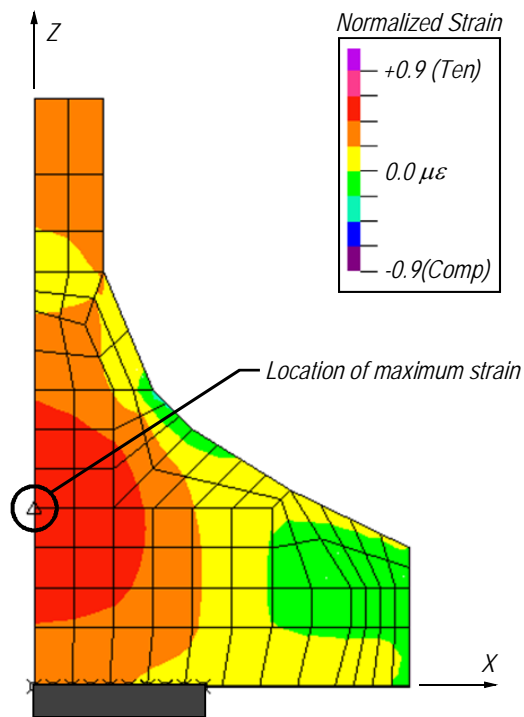


Figure 20–Normalized transverse (x-x) strain at end of FIB-8

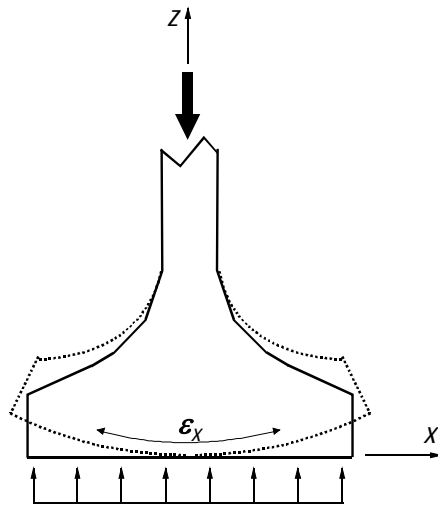


Figure 21–Flexural behavior

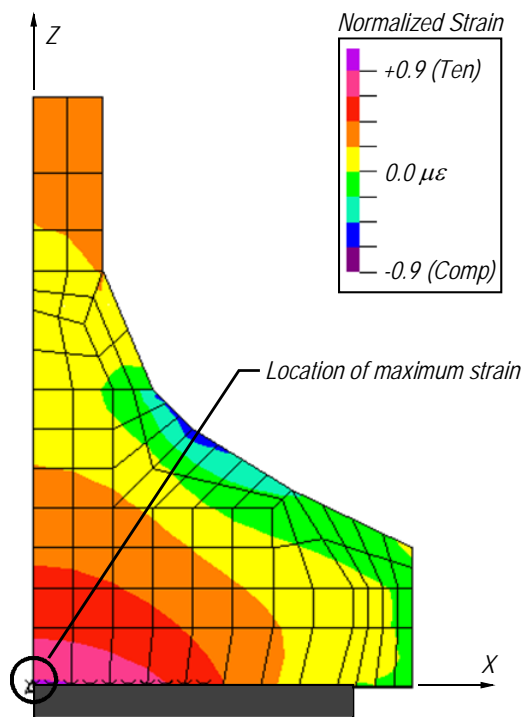


Figure 22–Normalized transverse (x-x) strain at end of FIB-16

To further investigate the relationship between transverse strain and bearing pad width, strain at three points on the end of the beam were plotted against the bearing pad width (Figure 23). Points were located at the end of the beam ( $Y=0$  in.) along the plane of symmetry ( $X=0$  in.) at  $Z$  coordinates of 0 in., 5 in., and 9 in. Looking first at the point  $Z = 0$  in., it can be seen that

the maximum transverse strain increased as the bearing pad width also increased. This condition was a consequence of flange-bending behavior. For the point at  $Z = 9$  in., the transverse strain increased as the bearing pad width decreased. Thus the strain at  $Z = 9$  in. was maximum when the beam experienced bursting behavior, and was smaller when flange bending dominated the behavior. The strain at  $Z = 5$  in. remained fairly constant as the pad width changed. The optimum bearing pad width, i.e. the width that minimized the transverse strain, was approximately 21 in. This coincides with the width where the behavior changed from bursting to flexural behavior.

Figure 24 shows the normalized transverse strains in the end region for four models with varying bearing pad widths. Variations in the transverse strain between the different models only occurred in portions of the beam adjacent to the bearing pad. In these portions of the beam, the ‘bursting’ and ‘flexural’ behavior were evident in both the Z-Y and Z-X planes. Regardless of pad width, the greatest transverse strains always occurred at the end of the beam.

Transverse strain distributions in the end region of the rectangular section are shown in Figure 25 for models with four different bearing pad widths. As previously noted, the transverse strains were normalized by  $\epsilon_{y,\max}$  from the FIB model. The scale and color contours are different from earlier figures of the FIB section. The figure shows that the magnitudes of the strains in the rectangular section were considerably less than for the FIB section. For instance, the maximum normalized transverse strain in the R-8 model was only 38% of the maximum from the FIB-8 model. For R-16, the maximum normalized transverse strain was only 14% of the maximum from model FIB-16.

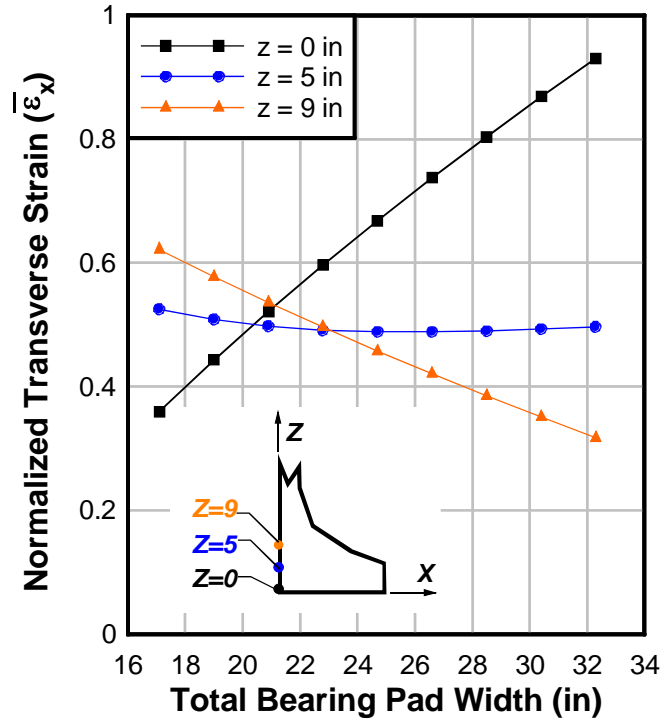


Figure 23–Normalized transverse (x-x) strain vs. bearing pad width

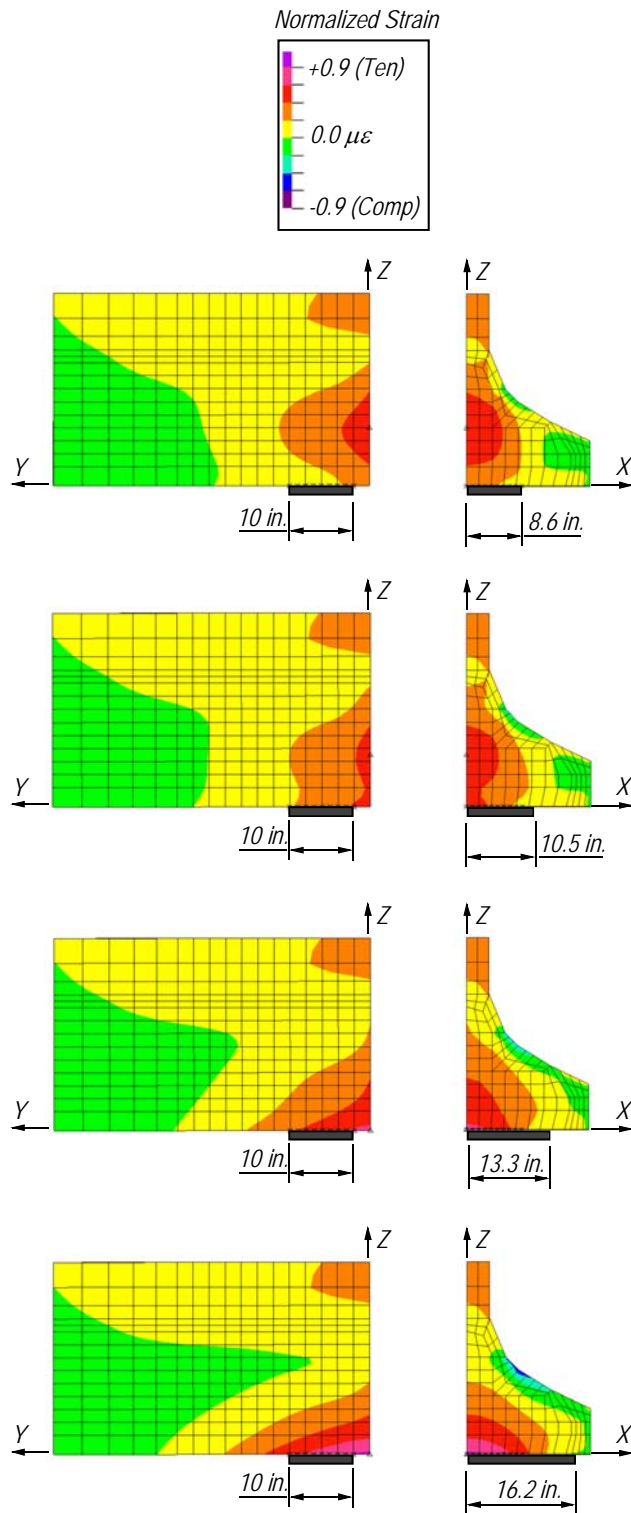


Figure 24—Normalized transverse (x-x) strain vs. bearing pad width in FIB

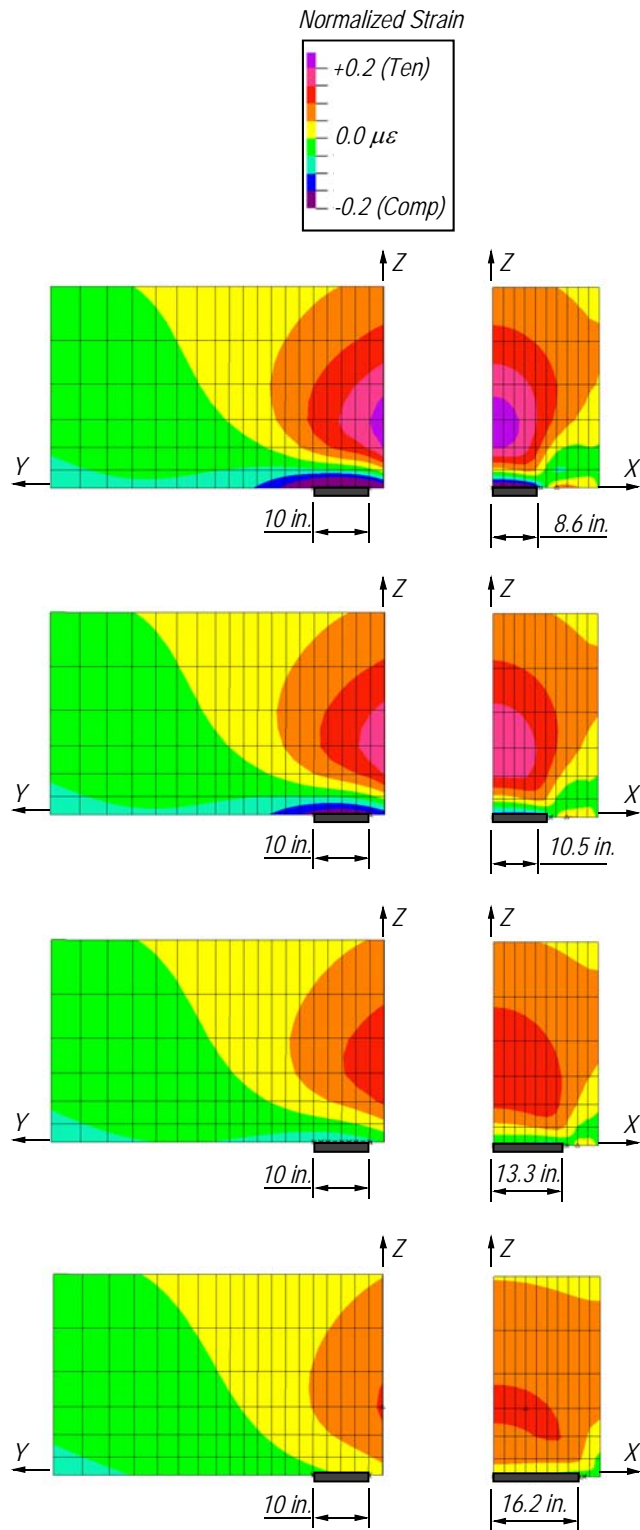


Figure 25–Normalized transverse (x-x) strain vs. bearing pad width in rectangular section

The greatest strain in the rectangular section models occurred in the model with the narrowest bearing pad. Conversely, the transverse strains were least in the model with the greatest pad width. Although the transverse strain varied as the pad width changed, the location of the maximum transverse strain always occurred at the end of the beam.

A parametric study of bearing pad width was also conducted using the small beam FE model (Figure 26). Results were similar to the FIB model. Regardless of bearing pad width, maximum transverse strain always occurred at the end of the beam. Under the flexural mode, maximum transverse strain occurred at the end of the beam at bottom of the section. For the bursting mode, maximum strain occurred at the end of the beam and at a distance of approximately 60% of the flange depth above the bearing pad. The transition between bursting and flexural behavior occurred when the bearing pad width was approximately twice the web width. This pad width also corresponded to the lowest value of peak transverse strain.

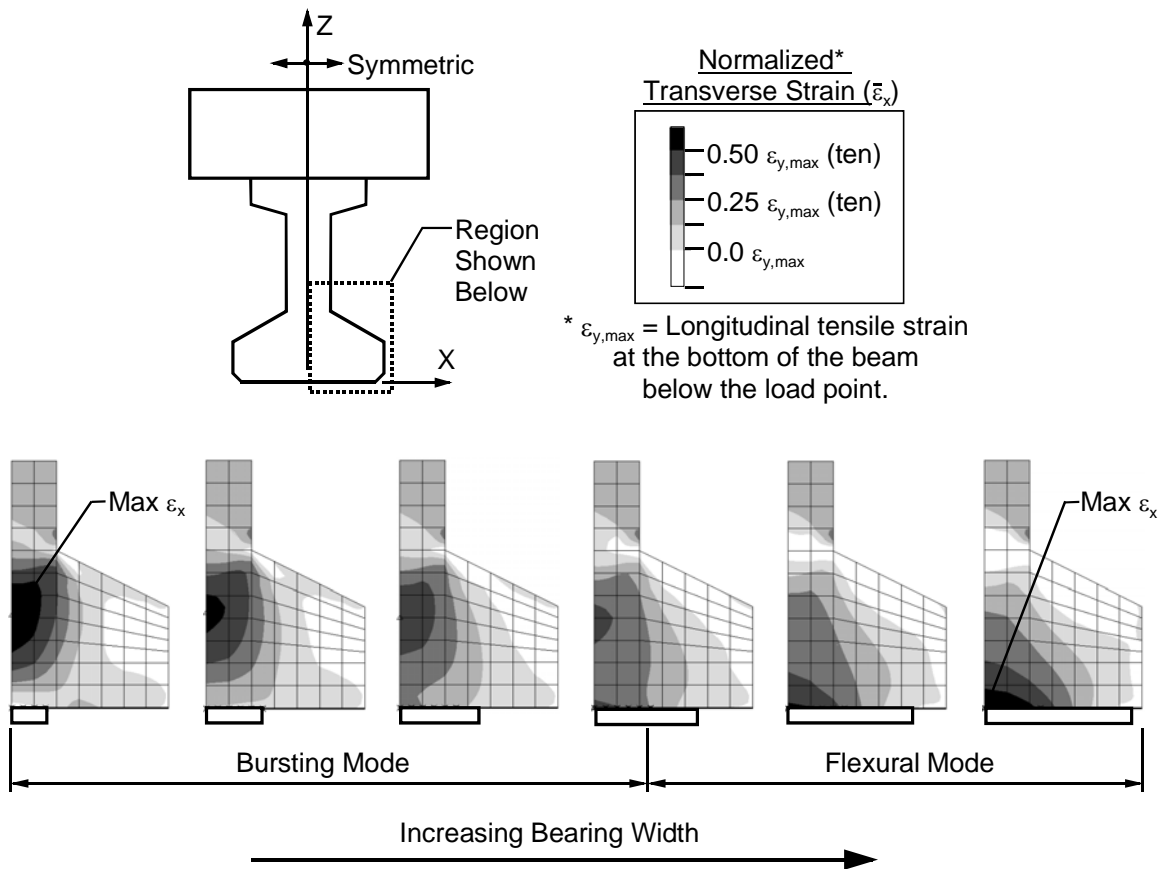


Figure 26–Normalized transverse (x-x) strain vs. bearing pad width in small beam

### 1.4.3 Effect of Steel Bearing Plate

The FDOT standard detail for the FIB end region specifies (FDOT 2009) a ½ in. thick x 12 in. x 36 in. steel bearing plate be embedded where the beam contacts the bearing pad. The bearing plate protects concrete in the region of high bearing stresses, and can be configured to aide in the constructability of skewed and/or sloped girders. Due to the location of the plate, its effect on the transverse (x-x) strain was of interest. To evaluate the effects of the bearing plate, the plate was added to the FIB models used in the previous section. The bearing plate was modeled with 4 node 2D shell elements positioned at the bottom of the beam (Figure 27). The bearing plate discretization was double that of the adjacent 27 node solid elements, thus each node from the plate elements aligned with a node from the adjacent solid element (Figure 28). Full composite behavior between the bearing plate and the concrete was assumed in the model. The parametric study of bearing pad width presented in the previous section was repeated for the model with the bearing plate.

Figure 29 shows the normalized transverse strain at the end of the beam vs. the bearing pad width for models with and without the steel bearing plate. As was done previously, the strain values in the figure were normalized by the maximum flexural tensile strain ( $\epsilon_{y,max}$ ) (Figure 18) below the load point. Figure 29 shows that the presence of the steel bearing plate reduced the transverse strain at point Z=0. At a bearing pad width of 17 in., the model with the bearing plate reported 20% less transverse strain at point Z=0 than the model without the bearing plate. The reduction in strain was more pronounced at greater pad widths. For example, the bearing plate model reported 33% less transverse strain at a bearing pad width of 32 in. Results also indicated that the influence of the bearing plate was limited to those portions of the beam closest to the plate. At point Z =9, the presence of the bearing plate had insignificant effect on transverse strain.

Figure 30 shows the transverse strain distribution for models with different bearing pad widths. Similar to the FIB model that did not include the bearing plate, Figure 30 shows that the bearing plate models also experienced ‘bursting’ and ‘flexural’ behavior for narrow and wide bearing pad widths, respectively.

When compared to the model without the bearing plate, the reduction of transverse strain is attributed to the additional confinement provided by the plate. This effect was most significant when the bearing pad was at its widest, and when the maximum transverse strain occurred

closest to the plate. The models evaluated the effect of the plate in the range of elastic behavior, and did not consider post-cracking behavior.

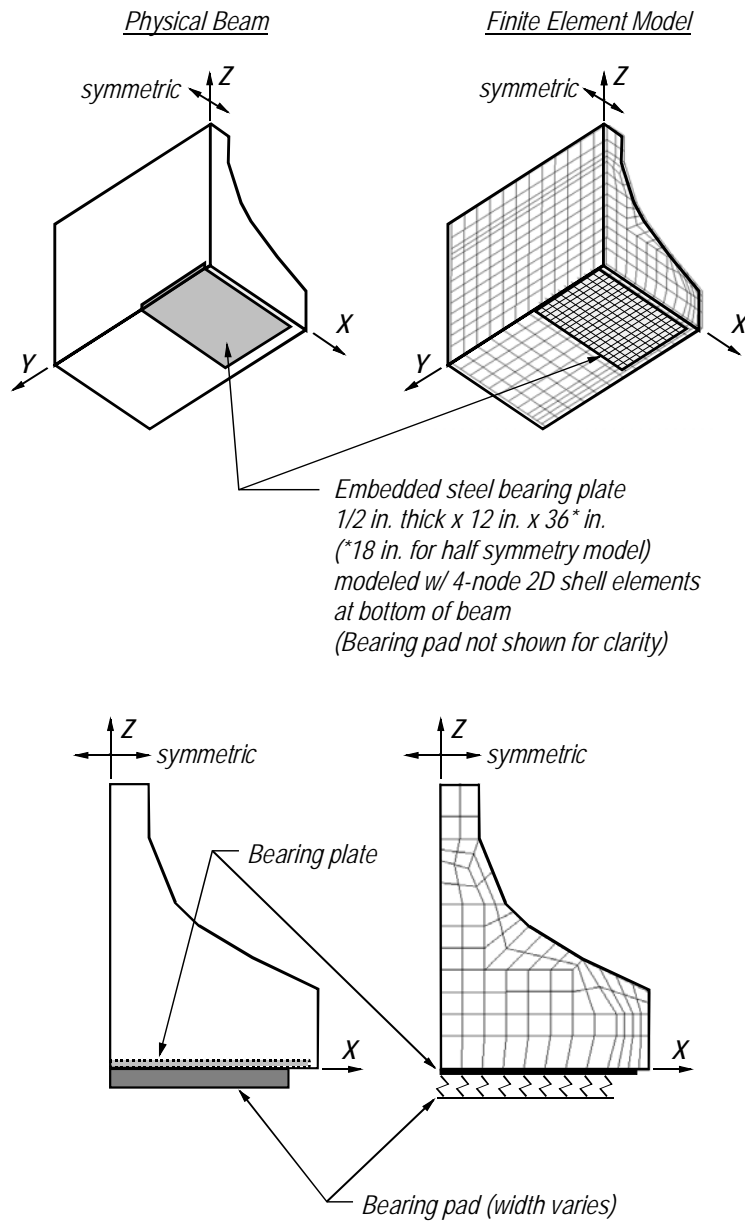


Figure 27–Steel bearing plate beam and model

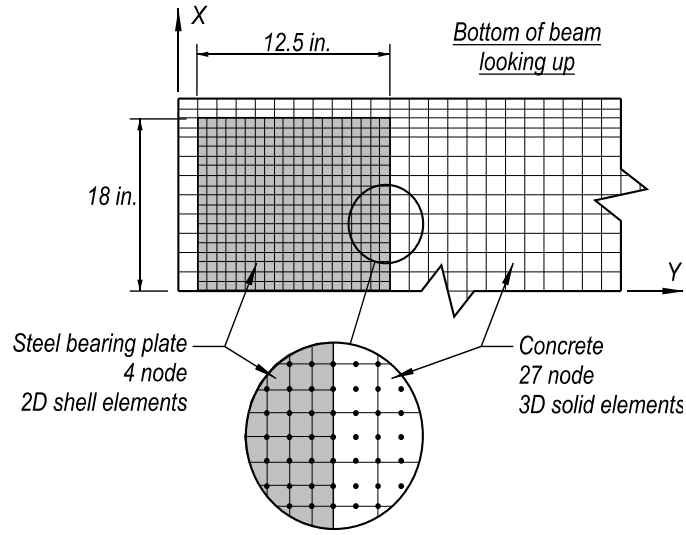


Figure 28–Bearing plate discretization

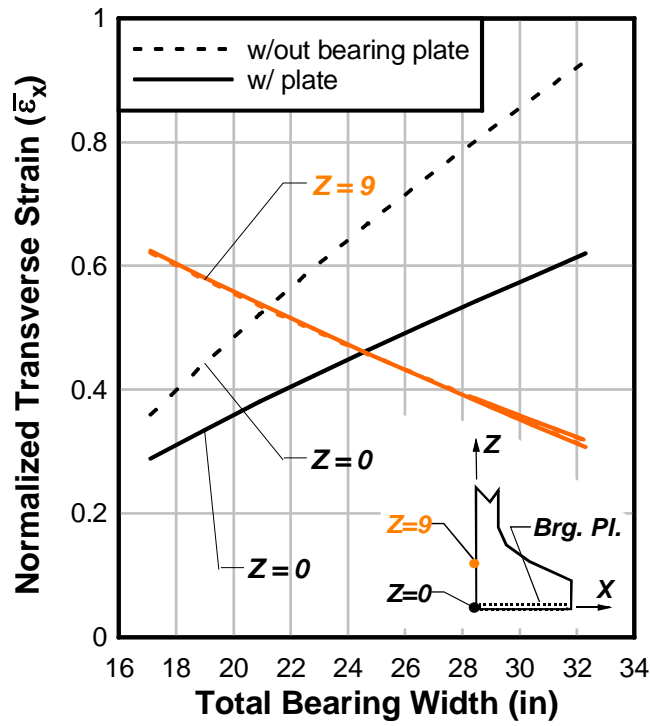


Figure 29–Effect of bearing plate and bearing pad width on transverse (x-x) strain

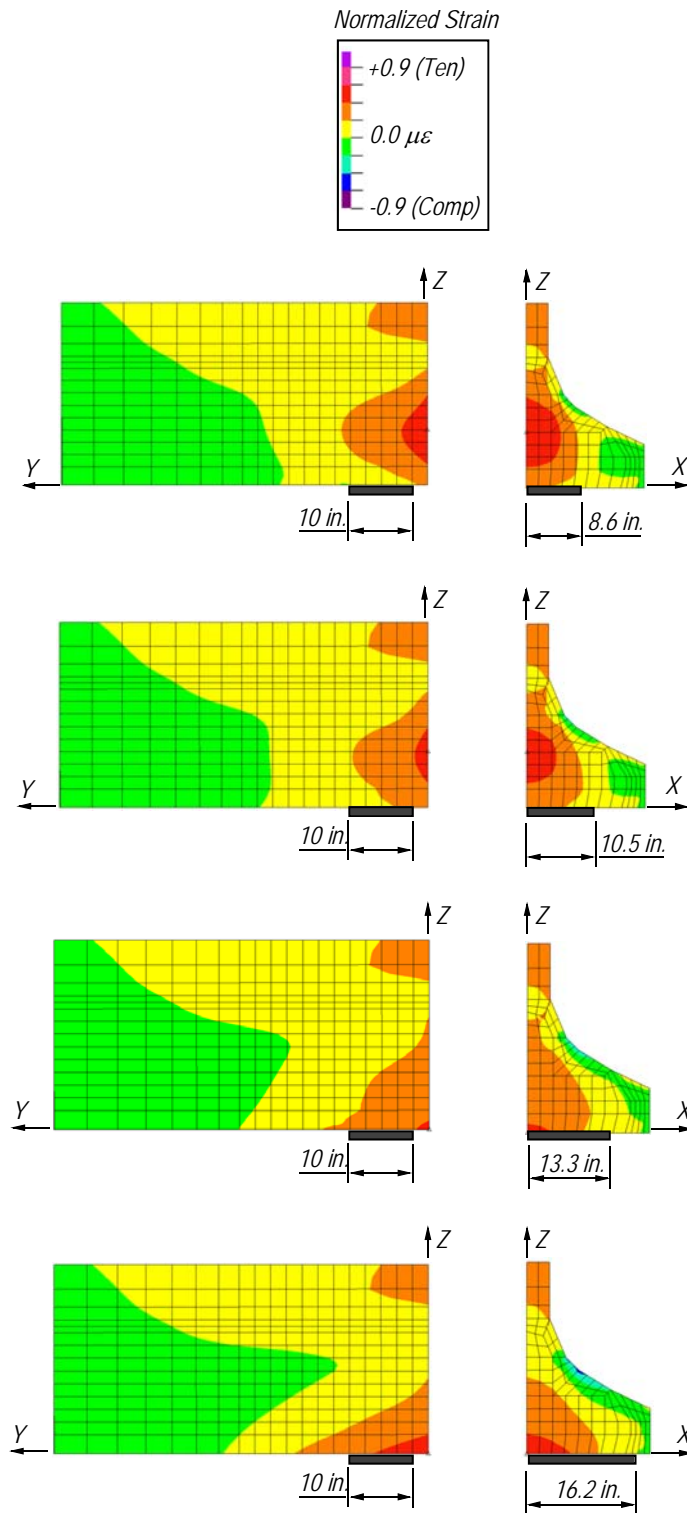


Figure 30–Normalized transverse (x-x) strain vs. bearing pad width in FIB section with steel bearing plate

#### 1.4.4 Bearing Pad Width Effect on Transverse Force

Small beam, FIB, and FIB with bearing plate FE models developed in previous sections were used to evaluate the relationship between bearing pad width and transverse force. As with all models in this chapter, the analysis was linear-elastic and considered the effects of applied loads only.

Transverse force was calculated by integrating transverse stress over the area shown in Figure 31. Boundaries of the integration area were selected to capture those portions of the girder near the bearing pad subjected to steep strain/stress gradients due to the reaction force, and to include portions of the bottom flange where confinement reinforcement is placed to carry transverse tension. Stress distributions beyond the integration area were not significantly affected by changes in bearing pad width. Analyzing transverse forces over the selected area gave a broad picture of pad width effects in the end region, whereas analysis of strain data in previous sections only looked at maximum effects and effects at discrete points.

The integration area used in transverse force calculation was located at the centerline of the considered cross-section. Dimensions of the integration area were determined as a function of the bottom flange width ( $W_f$ ) so that similar integration calculations could be conducted on beams with different geometries.

Discrete normal (x-x) stress values from center nodes in the integration area were multiplied by the associated y-z areas to obtain the transverse (x-x) force (Figure 32). Total transverse tensile force was taken as the sum of all element tensile forces. Compressive forces (when they occurred) were ignored in calculations of the total transverse force. This approach was taken because the transverse compressive forces were assumed to be resisted by concrete and transverse tensile forces resisted by confinement reinforcement.

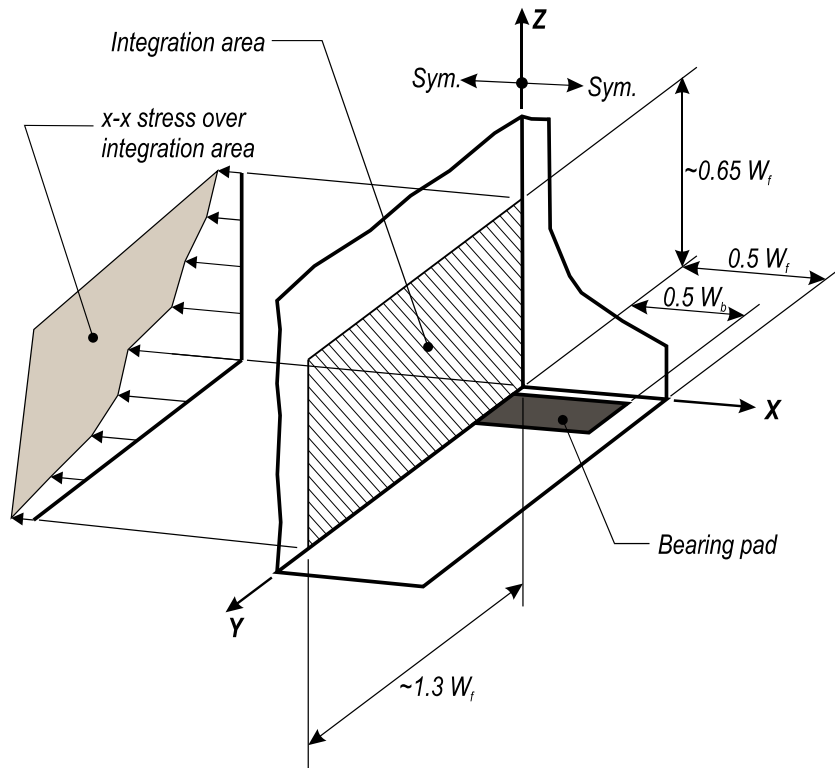


Figure 31–Integration area for transverse force

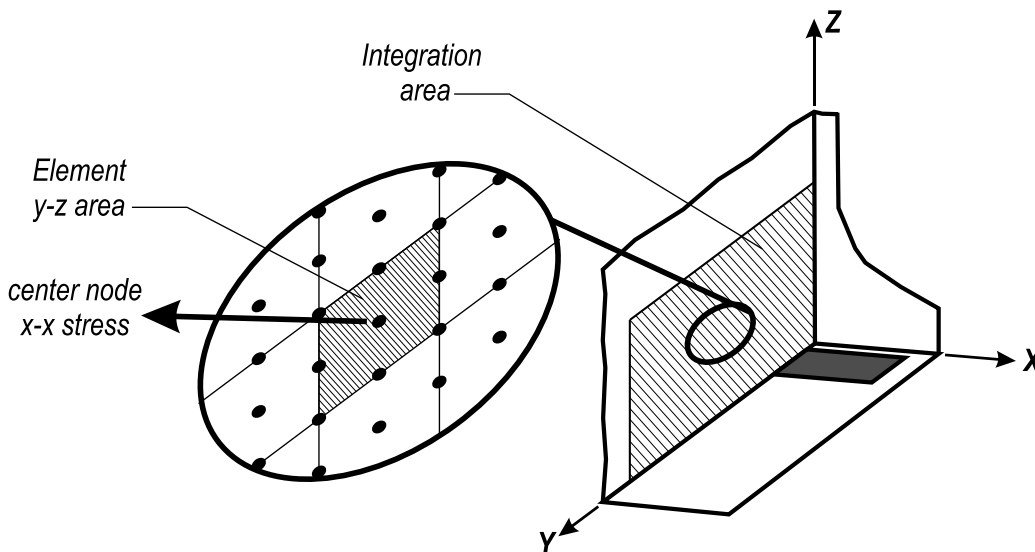


Figure 32–Element x-x stress and y-z area

Figure 33 presents the variation in net transverse tensile force as a function of the bearing pad width in the FE models. For the considered models and geometries, the transverse force was equal to 13% to 28% of the reaction force. Transverse force was smallest relative to the reaction

force when the bearing pad width was approximately 60% of the flange width. This ratio of bearing-to-flange width also corresponded to the change in behavior between bursting and flexural behavior as discussed in previous sections. For bearing pad-to-flange width ratios greater than 0.5, the FIB model including the bearing plate had the lowest normalized transverse force. This is attributed to the stiffness of the bearing plate, which attracted transverse force when the bearing pad width approached the flange width. Transverse force in the bearing plate is not included in the data presented in Figure 33.

FDOT design standards (FDOT 2009) for FIB girders resulted in a bearing pad-to-flange width ratio of 0.84. For this ratio, the calculated transverse tensile force in the bottom flange was equal to approximately 25% of the reaction force in the model without a plate, and approximately 17% of the reaction force in the model with a plate. These relationships reflect linear-elastic behavior and would likely change after cracks form in the bottom flange.

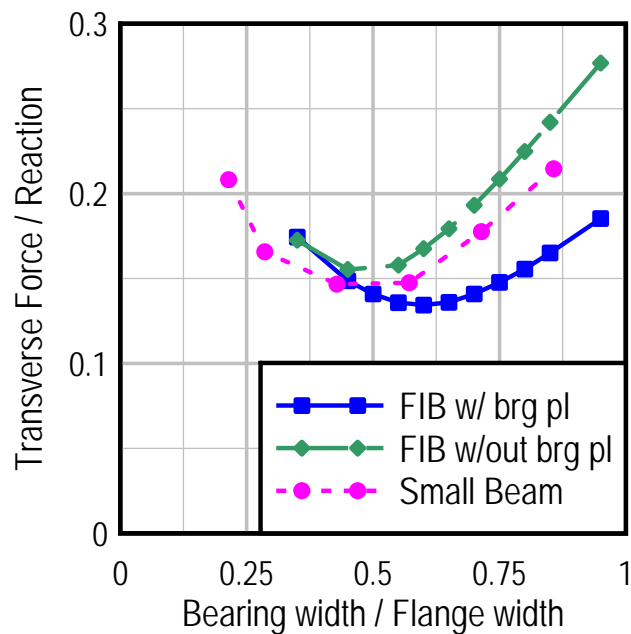


Figure 33–Net transverse (x-x) tensile force vs. bearing geometry

### 1.5 Summary and Conclusions

Linear-elastic FE models were used to evaluate the effects of applied load on I-beam and rectangular shaped end regions. Variables in the models included bearing pad width, bearing pad stiffness, cross-section shape, and the presence of embedded steel bearing plates. The following conclusions are based on results of the evaluations:

- The location of maximum transverse strain occurs at the end of the beam regardless of bearing conditions or cross-section.
- Due to Saint Venant's principle, changes to the bearing conditions have little effect beyond those portions of the beam nearest to the bearing.
- For the range of stiffness values reported for neoprene bearing pads, variations in pad shear stiffness have negligible effect ( $< 0.1\%$ ) on the transverse strain in the end region. However, variations in pad axial stiffness can change the transverse strain by  $\pm 3\%$ .
- Depending on the width of the bearing pad, two types of strain distributions (behaviors) occur in the end region I-girders. A behavior denoted as 'bursting' occurred when the bearing pad width was narrow, and the transverse strain was distributed in a bottle-shaped manner. However, 'flexural' behavior occurred when the pad width was large, and transverse strain was dominated by flexural strains in the flange.
- When 'flexural' behavior occurred, the transverse strain increased as the bearing pad width increased.
- When 'bursting' behavior occurred, the transverse strain increased as the bearing pad width decreased.
- The transition between 'bursting' and 'flexural' behavior occurred when the bearing pad width was approximately equal to 60% of the bottom flange width. This pad width also corresponded to the optimal width for minimizing transverse tensile strain.
- The magnitudes of transverse strain in rectangular sections were 14% to 38% of those in similarly dimensioned I-shaped flanged sections. This reduction in transverse strain was one of the benefits of using end blocks on girders with I-shaped sections.
- When the bearing pad width was less than the web width (as in the rectangular models), the transverse strains increased as pad width decreased.
- Steel bearing plates reduced the magnitude of transverse strain in the concrete nearest to the plate location. This effect was most pronounced when the bottom flange was acting in the 'flexural' mode.

- Transverse force in the bottom flange above the bearing pad and due to applied load was minimized when the bearing pad width was approximately equal to 60% of the flange width.
- For the conditions investigated in this analytical study the transverse force in the bottom flange above the bearing pad was approximately 25% of the reaction force.

## 2 Modeling of End Region during Prestress Transfer

This chapter presents FE modeling that was conducted to 1) provide a better understanding of the elastic behavior of the end region during and immediately after prestress transfer, 2) quantify lateral forces in the bottom flange within the end region, and 3) evaluate the effects of variables such as transfer length and embedded steel bearing plates on end region behavior. The FE program ADINA (R&D 2009) was used to conduct the modeling. Analyses were conducted using linear elastic properties and were intended to model pre-cracked behavior. Strain gage and displacement data from construction of girders H and V from Appendix D were used to validate the FE model. The Hoyer effect was not considered in analyses presented in this section, but is addressed in Appendix G as part of the development of the end region design model.

### 2.1 Model Configuration

Figure 34 shows the coordinate system used for FE models in this chapter. The FE model configuration was designed to be computationally efficient, yet able to capture the overall behavior of girders as well as local behavior of the end region. Distribution of transverse ( $x-x$ ) tensile strain in the bottom flange was of particular interest

Behavior during and immediately after prestress transfer was modeled as shown in Figure 34b. Transfer of prestress created negative bending moments of sufficient magnitude to overcome girder self-weight and cause the girders to camber upward. At this stage the boundary conditions were selected such that the girder model had vertical ( $Z$ -direction) supports at each end. While friction forces generally develop between test girders and the stressing bed, friction forces were assumed to be small and were thus neglected in development of the FE model. The restraining force from uncut strands was also assumed to be negligible. These assumptions appear valid based on comparison with experimental data, as presented in the next section.

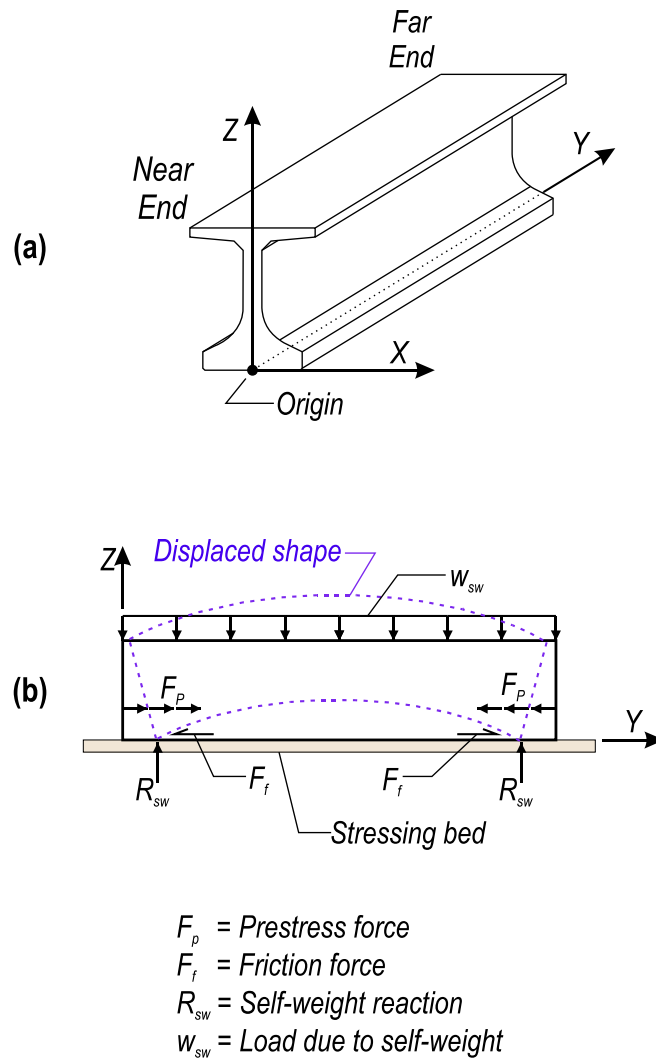


Figure 34—Coordinate system and free-body diagram of girder after prestress transfer

Figure 35 shows the details of the FE model and boundary conditions used to analyze the girder. A rectangular mesh of 27-node 3D solid elements was used to build the portion of the model representing the end region. The portion of the model that used solid elements was selected to fully capture the effects of the prestress and bearing forces on the end region. Beam elements were used in the remainder of the beam with the transition from beam to solid elements made using rigid 2D shell elements and 1D rigid links. Rigid shell and link elements coupled the displacements of the 3D solid elements with the displacements and rotations of the 1D beam elements. Transitioning to beam elements reduced the computational demand while still modeling the global girder behavior and boundary conditions. Beam elements were placed at the centroid of the cross-section and were assigned cross-sectional properties equivalent to the FIB-

54 test girders. A rigid link was provided to connect the beam elements to the physical location of the bearing at the bottom of the girder at the far end. The embedded steel bearing plate at the near end was modeled using shell elements.

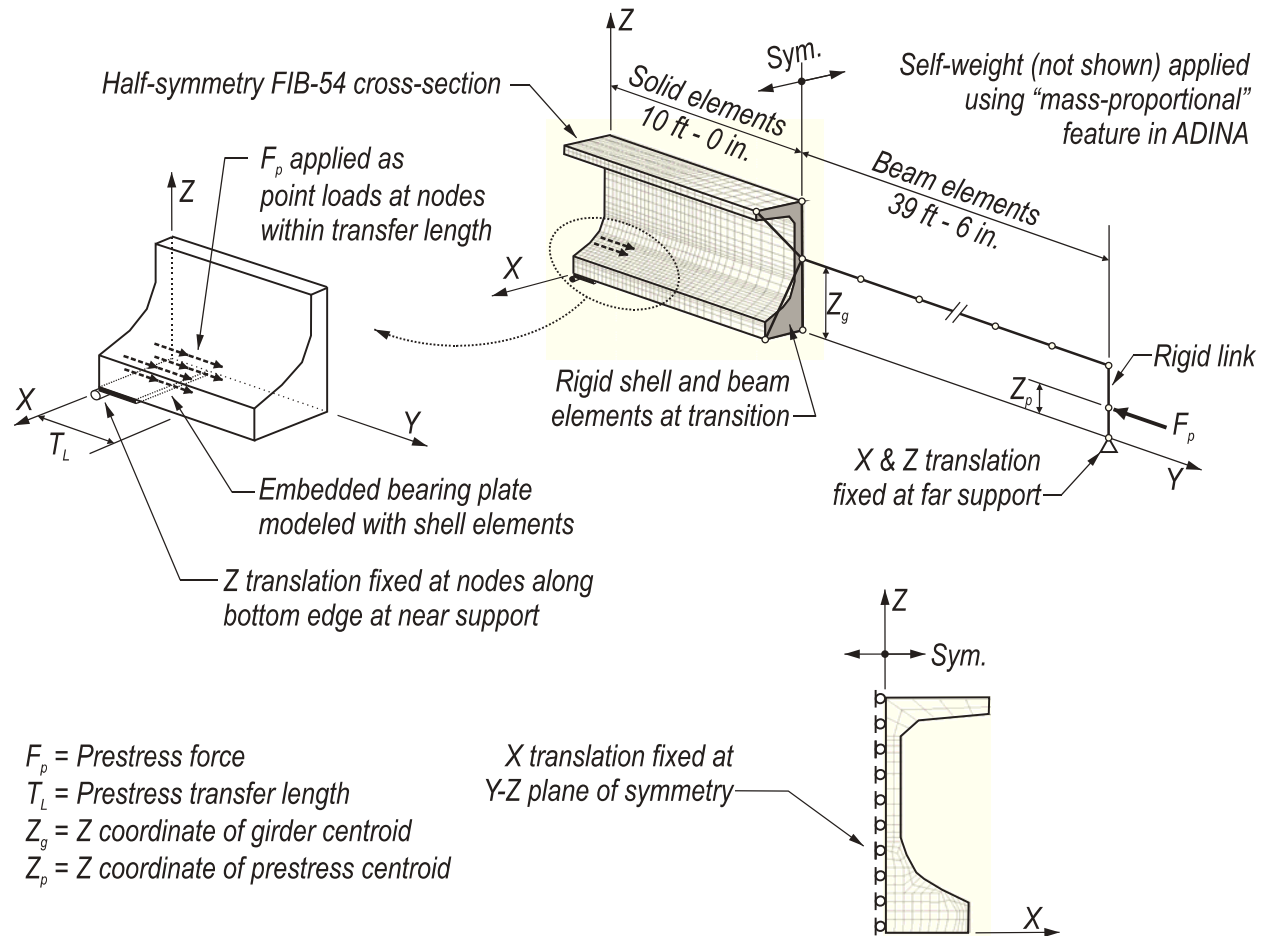


Figure 35-FE model details

Boundary and loading conditions of the FE model were consistent with the conditions of the physical test girders during and after prestress release. Vertical displacement was restrained along the bottom edge of the model at the near support and at the bottom of the rigid link at the far end. Prestressing forces were applied to both ends of the model. Application of prestressing at the near end is discussed in detail later in this section. At the far end, prestressing was applied as a single point load at a height equal to the Z-centroid of the prestressing force.

The cross-section, boundary conditions and loads were symmetrical about the Y-Z plane, allowing for half of the beam to be considered in the FE model. As such, transverse (x-x) translations were restrained at all nodes on the plane of symmetry.

Self-weight was modeled using the “mass-proportional” load feature in ADINA. This feature was employed by assigning mass density to the materials in the model, and assigning the direction and magnitude of gravity, and then allowing ADINA to calculate the body forces associated with self-weight.

The FE model was developed such that nodes in the bottom flange mesh aligned with the prestressing strand layout. Because element nodes coincided with the strand locations, the prestressing force could be applied as point loads to nodes within the transfer length (Figure 35). Prestressing in the FE model was based on test girders H and V that contained (39) fully bonded 0.6-in. diameter prestressing strands (Figure 36). Prestressing forces occurring at the centerline of the cross-section (plane of symmetry) were reduced by 50% to account for the model symmetry. Forces from the partially debonded strands were not included in the model. This simplification appeared reasonable based on the validation presented in the next section. It is further justified by considering that the partially debonded strands in the test girders did not transfer loads within the end region, which was the area of primary interest. Individual steel strands were not explicitly included in the model.

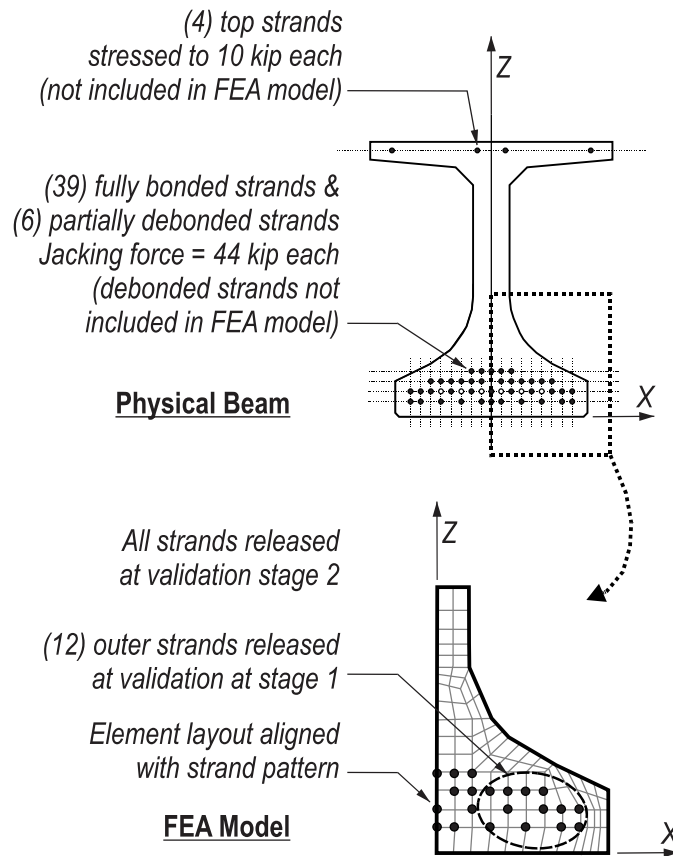


Figure 36–Strand layout and element mesh

A transfer length of 17.5 in. was used. This length was approximately half of the transfer length calculated using AASHTO LRFD provisions. A shorter length was used for multiple reasons. First, strand transfer lengths were shortest during and immediately after transfer (Barnes et al, 1999), which was the time that strain data were taken for validation. Second, the AASHTO LRFD transfer lengths were conservatively long relative to experimental data (Barnes et al., 1999). The transfer length in the FE model was denoted as  $T_L$  to distinguish it from the physical and code calculated transfer lengths.

Based on experimental data, the elastic prestress loss after all strands were released was approximately 10%. Elastic loss was indirectly considered in the FE model by reducing the magnitude of the applied prestress forces. As with the test girders prestress forces were applied sequentially to the model. As additional forces were applied, the elastic loss was assumed to be proportional to the number of released strands. To demonstrate how elastic losses were applied,

Table 5 lists some of the stages of prestressing, prestress forces and elastic losses considered in the FE model.

Table 5–Application of elastic loss

Stage	Initial prestress force	Assumed elastic loss (percentage)	Assumed elastic loss (force)	Prestress applied to model (initial minus losses)
4 of strands released	176 kip	2.0%	3.5 kip	172.4 kip
10 (half) strands released*	440 kip	5.0%	22.0 kip	418.0 kip
17 strands released	748 kip	8.7%	65.0 kip	683.0 kip
All strands released**	1716 kip	10.0%	171.6 kip	1544.4 kip
*Verification stage 1				
** Verification stage 2				
All forces for half symmetry FIB-54 model				

The concrete modulus of elasticity for each model was set at 4700ksi, and the Poisson’s ratio was set at 0.2. The modulus of elasticity value was chosen to match tested material properties from test girders used for validation.

The model configuration was validated by comparison with experimental data, and was then used in more general investigations of the stress and strain state in the end region. Details of the verification and validation are contained in the next section.

## 2.2 Model Validation and Verification

A verification study was conducted to determine that the mesh used in the proposed FE model had sufficient density to capture the end region behavior. Figure 37 shows the proposed mesh density and a refined mesh density, which was used for comparison. The refined mesh was twice as dense (i.e. 4 times more elements) as the proposed mesh.

Principal tensile stress results from the proposed and refined models are compared in Figure 38. Differences between refined and proposed meshes occurred primarily in elements adjacent to the applied prestress forces. Locations away from the prestress forces had similar stress magnitudes and distributions for both meshes. Based on this comparison the proposed mesh was deemed acceptable for evaluating behavior away from the prestress forces, and the refined mesh was required for evaluations near the prestress forces.

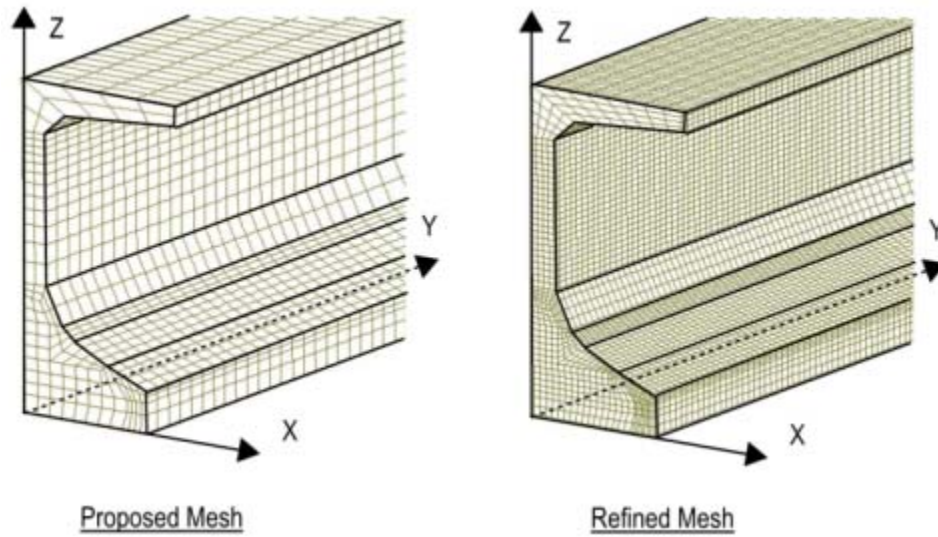


Figure 37–Verification study mesh densities

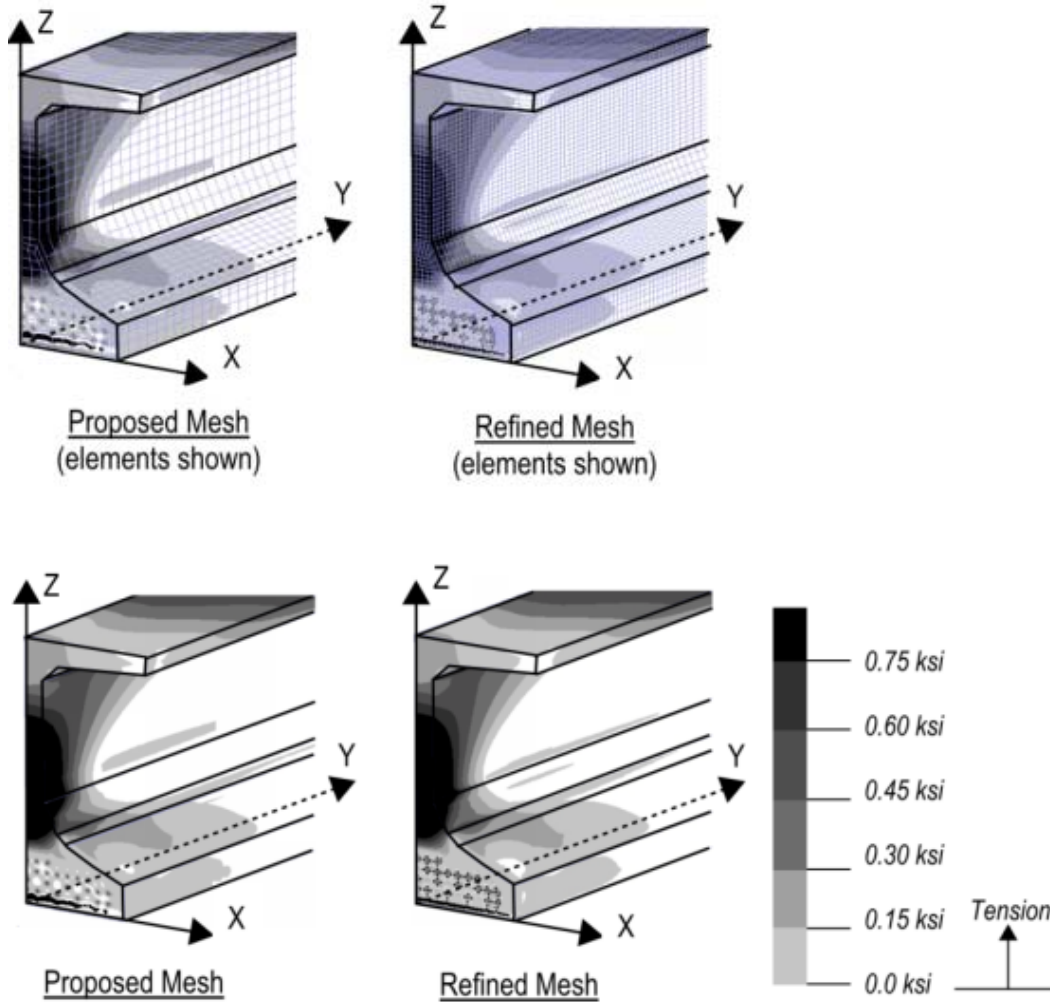


Figure 38–Verification study principal tensile stresses

Test girders H and V were selected for use in validating the FE model. During prestress transfer in these, strands farthest away from the girder centerline were cut first with subsequent strand cuts made progressively closer to the centerline. Based on the release pattern, two stages were considered in the model validation. During stage 1 only the outer strands were released. During stage 2 all strands were released.

Comparisons with the experimental data indicate that the FE model did an adequate job of capturing both the global and local linear elastic behavior of the physical test beams. The exaggerated displaced shape calculated by the FE model is shown in Figure 39 for stage 2 (all strands cut). Camber at mid-span calculated by the FE model was 0.90 in., which was within 2 % of the experimentally measured camber of 7/8 in.

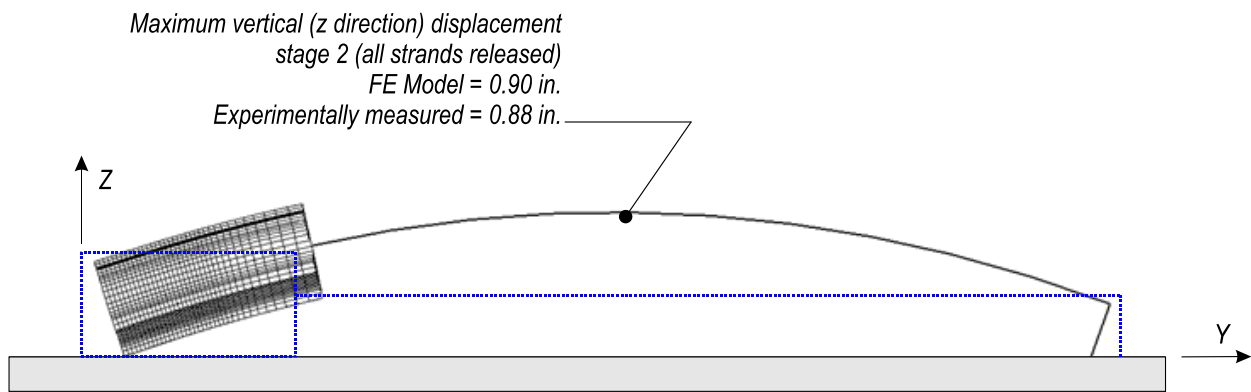


Figure 39–Displaced shape

Although cracking was not observed visually during or immediately after prestress transfer in girders H and V data from strain gages indicated that cracking may have occurred in the physical girders as the prestressing strands were being cut. Figure 40 shows that the magnitude of tensile strain reported by the gages exceeded the expected concrete rupture strain of 132 microstrain. The expected rupture strain was derived from empirical relationships for elastic modulus and rupture strain in ACI 318 (2011). Based on the location and magnitude of the tensile strains calculated by the FE model, it is not surprising that strain gages reported strains greater than the expected cracking strain. This result suggests that the FE model captured the behavior of the physical girders at both stages of prestress transfer.

With the exception of the locations presented in Figure 40, the calculated linear-elastic FE model strain values at most locations were below the experimental rupture strain. Experimental data from most strain gages also demonstrated linear-elastic behavior. Data from these gages were used to validate the linear-elastic strains calculated by the FE model.

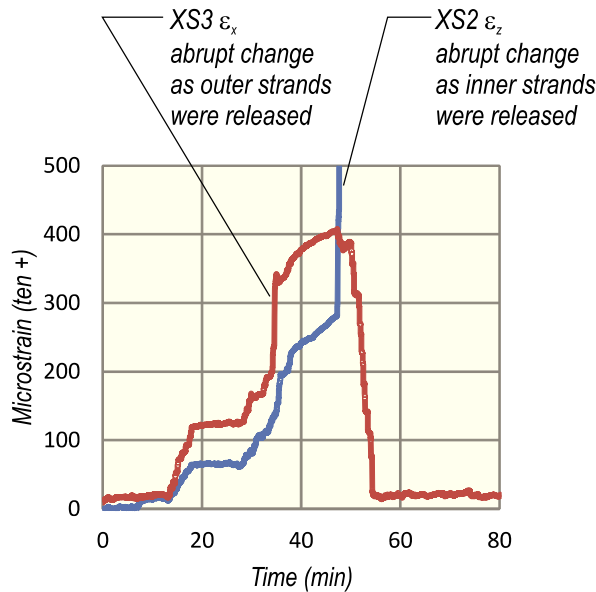
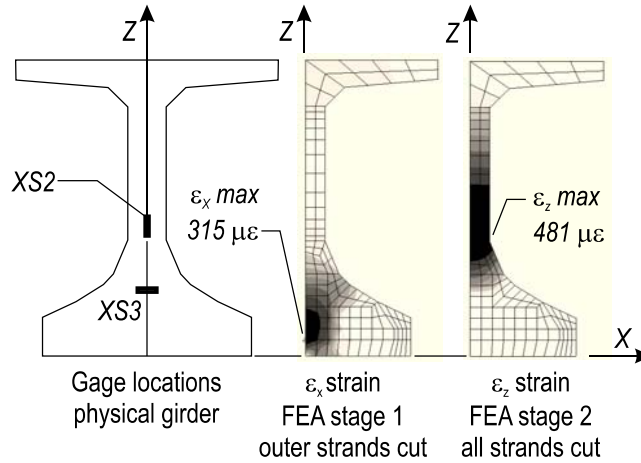


Figure 40–Comparison of experimental and FE model strains at cracks

Transverse (x-x) strain was of particular interest because transverse concrete behavior is coupled with confinement reinforcement behavior. Strain data from gages embedded in the physical girders are presented in Figure 41 along with strain data from the FE model. As demonstrated in the figure, the FE model was in good agreement with the experimental data

throughout the end region and at both stages. Gages located at  $Y = 2$  in. were near the cracking that occurred prior to stage 1, hence the variability in those data points.

Longitudinal (y-y) strains at the edge of the bottom flange are compared in Figure 42. Strains predicted by the FE model were within the scatter of the strain data at stages 1 and 2. The good agreement between the FE model and the longitudinal experimental data suggest that the transfer length used in the model (17.5 in.) was consistent with the transfer length in the physical girders.

Figure 43 compares the vertical (z-z) strain from the FE model and the test girders. Trends and magnitudes were consistent between FE model and experimental data. The largest vertical strains occurred at the end of the girder ( $y = 0$  in.) Vertical strains were larger during stage 2 than stage 1.

Strain and displacement data from the FE model were in good agreement with experimental data. The occurrence and location of cracking in the experimental girders were consistent with the locations of maximum tensile strains calculated by the FE model. It was concluded that the model accurately captured the global and local behavior of the physical girders at multiple stages of prestress transfer and that the model was adequate for more general parametric studies.

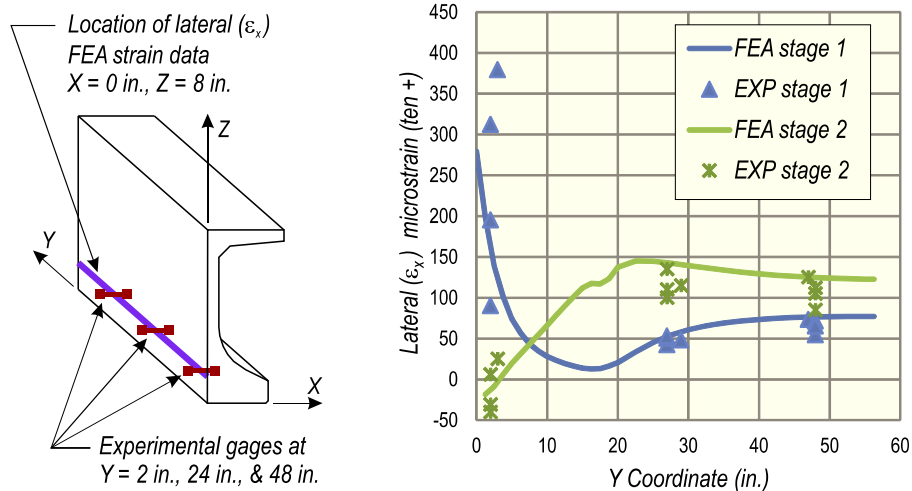


Figure 41–Comparison of experimental and FE model transverse (x-x) strain

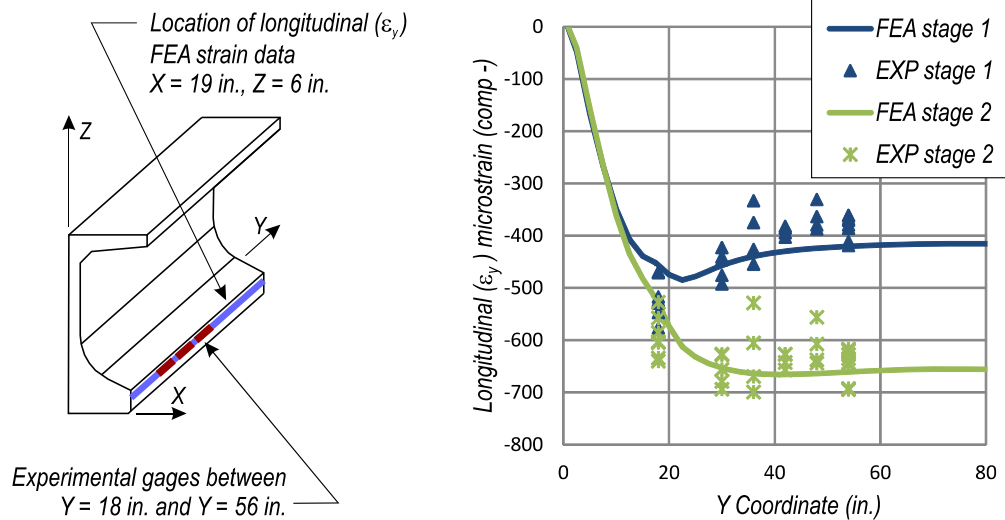


Figure 42—Comparison experimental and FE model longitudinal (y-y) strain

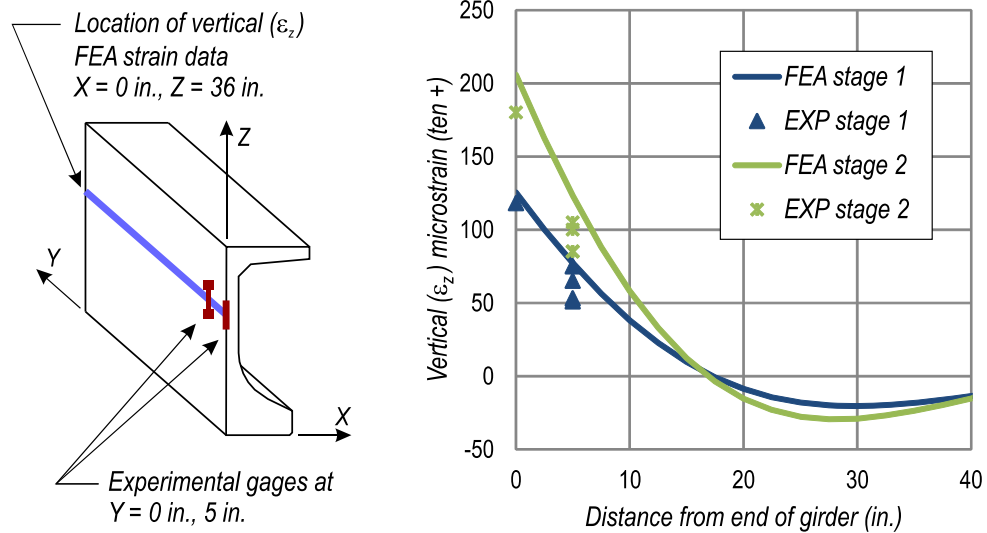


Figure 43—Comparison of experimental and FE model vertical (z-z) strain.

### 2.3 Transverse Force Quantification

Transverse tension forces in the bottom flange at the near support were of interest because they are resisted by confinement reinforcement in the event that the concrete cracks. This section describes the procedure used to quantify the transverse (x-x) force from the validated FE model.

Transverse force was calculated by integrating transverse stress over the area shown in Figure 44. This was the same area previously used for investigating the effects of bearing pad

width (Figure 32). Boundaries of the integration area were selected to capture those portions of the girder end subjected to steep stress gradients due to prestressing. Boundaries were also selected to include portions of the bottom flange where confinement reinforcement is placed to carry transverse tension. Boundaries of the integration area were defined as a function of bottom flange width ( $W_f$ ) so that similar integrations could be performed on girders with varied cross-sections.

Discrete x-x stress values from center nodes in the integration area were multiplied by the associated y-z areas to obtain transverse forces (Figure 45). The total transverse tensile force was calculated as the sum of all element tensile forces. Lateral force in the steel bearing plate was calculated in a similar manner. Compressive forces (when they occurred) were ignored in calculations of transverse force. I.e., transverse tensile force equaled the gross tension and was not reduced by compressive forces. This approach was taken because transverse compressive forces are supported by concrete and do not typically lead to cracking of concrete or tension loading of confinement reinforcement.

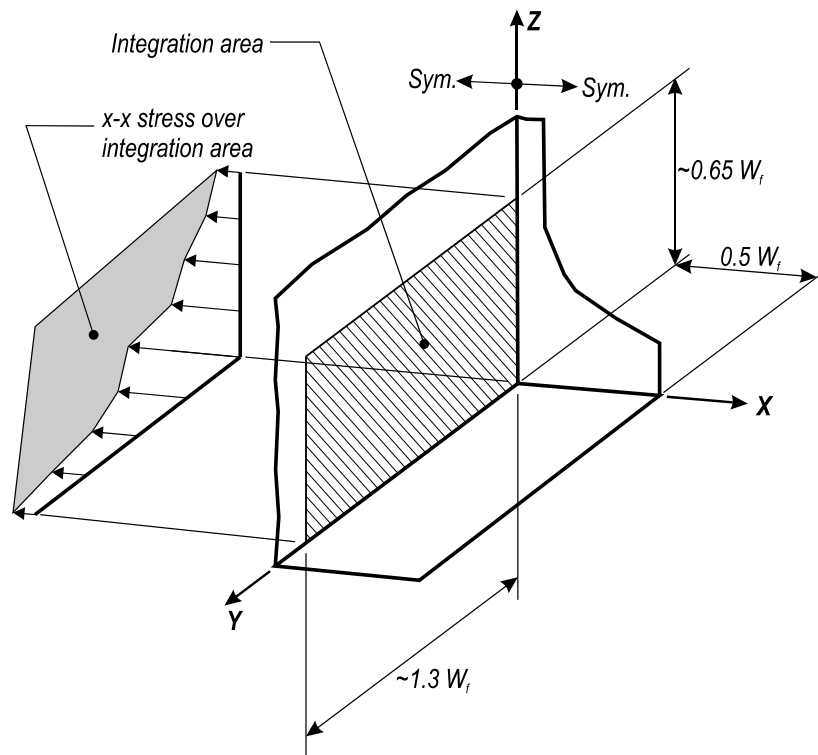


Figure 44—Area over which stress was integrated to determine lateral force

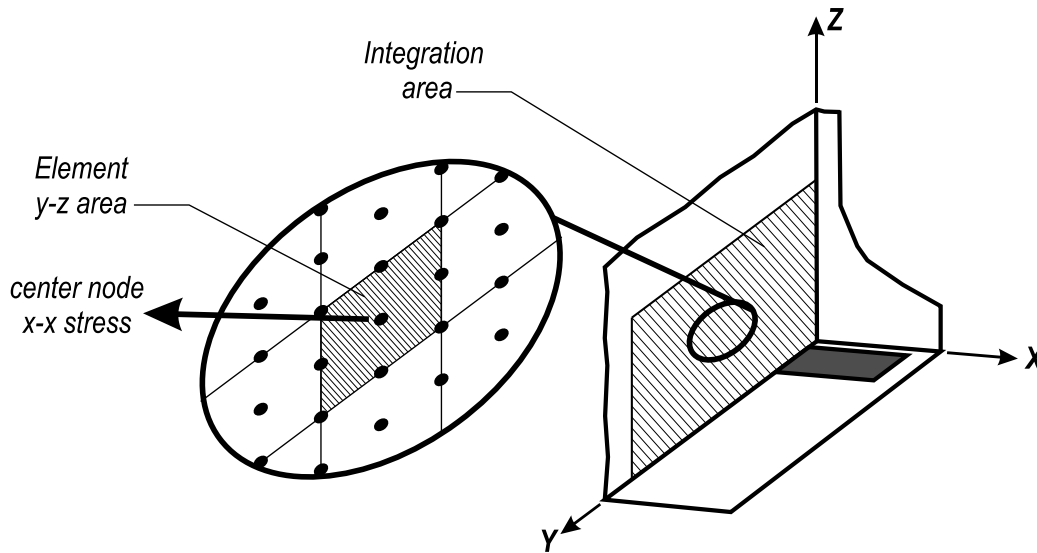


Figure 45–Element x-x stress and y-z area

## 2.4 Parametric Studies

### 2.4.1 Strand Release Parametric Study

Transverse (x-x) stresses and forces changed throughout prestress transfer as strands were sequentially cut. A parametric study was conducted to investigate the relationship between transverse force and the quantity of cut strands. This study used FE models of girders with FIB-54 and AASHTO Type IV cross-sections. The AASHTO girder model had the same configuration as the FIB model (Figure 35), with the exception of having cross-section dimensions of an AASHTO Type IV girder. Prestressing forces were applied as point loads over a transfer length of 17.5 in. Steel bearing plates were not included.

Elastic prestress losses were considered in the models. Losses were assumed to vary linearly from 0% when no strands were released to 10% when all strands were released. This magnitude of elastic loss was consistent with experimental data from girders H and V.

Strands in the experimental FIB girders were released from outside-in and bottom-to-top. To model this process, prestressing forces were added sequentially to FE models beginning at the location of outermost strands. Figure 46 show the locations of prestressing forces at different phases of prestress transfer in the FIB-54 model. Transverse (x-x) stress distributions are also shown. When only outer strands were released, the tensile stresses were concentrated within 10 in. of the girder end. Tensile stresses reduced in magnitude, but occurred over a greater portion

of the integration area after inner strands were released. Stresses shown in the figure were due to prestressing forces and self-weight.

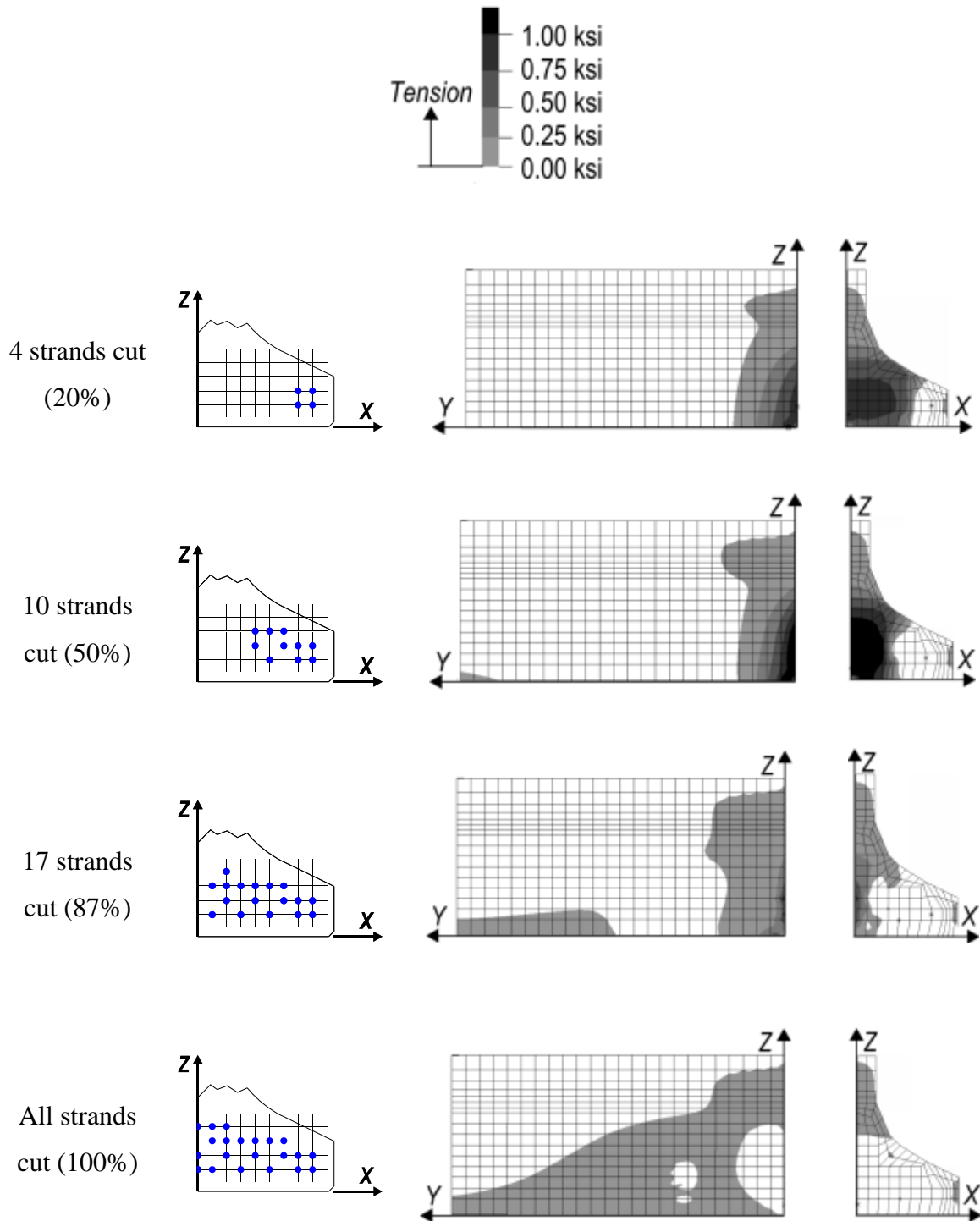


Figure 46–Transverse (x-x) stress at stages of prestress transfer

The bottom flange of the AASHTO Type IV section houses fewer strands than the FIB bottom flange. To normalize this difference, the quantity of strands in both AASHTO and FIB

models was designed to be approximately 50% of the maximum possible strand quantity for the given section. Strand locations in the FIB model also matched the experimental girders H and V.

The transverse tensile force at the cross section centerline was calculated at each stage of prestress release following the previously described integration procedure. Calculated forces are plotted as a function of the percentage of cut strands in Figure 47. The calculated forces presented in the figure were normalized by the final prestress force for each girder.

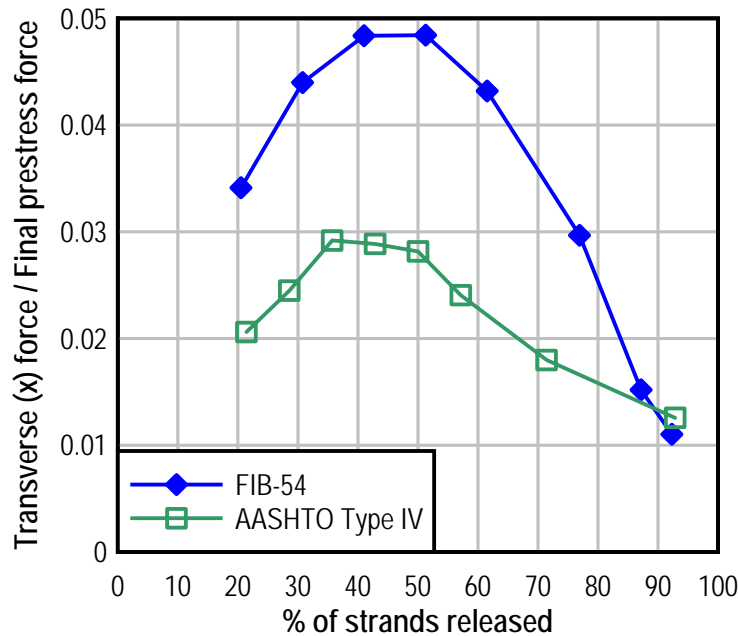


Figure 47–Variation in transverse force as strands are cut

For both girders the largest transverse tensile force occurred when approximately 40% of the strands were released. This percentage corresponds to the stage when only the strands in the outer portion of the flange had been cut. Transverse force decreased as the inner strands were cut. This observation is consistent with experimental strain data that reported the largest transverse tensile strains when the outer strands were released and a commensurate reduction in those tensile strains as the inner strands were released.

The FIB-54 model had higher ratios of transverse force to final prestress force than the AASHTO Type IV model. This was attributed to the FIB section’s relatively wide and slender bottom flange. Because of the greater width, strands in the FIB flange had a greater moment arm about the cross section centerline than did strands in the AASHTO flange.

Figure 47 also demonstrates the problem of partially debonding inner strands and fully bonding outer strands. In this circumstance, inner strands do not transfer prestress force at the end of the girder and consequently do not reduce the transverse tensile force at the centerline. This situation occurred in the experimental program in specimens FN and FB. Flange splitting cracks formed at the end of these girders at the centerline of the cross section. A similar situation and similar cracks were observed in experimental AASHTO Type IV girders by Llanos et al. (2009).

#### 2.4.2 Bearing Plate Contribution

The validated FE model was used to evaluate transverse force carried by embedded steel bearing plates due to prestressing forces. This evaluation considered the same stages of prestress transfer as were used in model validation. For stage 1 only the outer strands were released. For stage 2 all of the strands were released. The presence or absence of the steel bearing plate was also included as a variable, resulting in four unique variable combinations.

Figure 48 and Figure 49 present the transverse (x-x) stress distributions along the plane of symmetry for each of the four variations considered. Transverse force was calculated using the previously described integration procedure. Table 6 lists the maximum stresses and total forces of each model variation. Calculated force in the bottom flange was approximately 67 kip at stage 1. When the steel bearing plate was present, it attracted approximately 7 kip, or 10% of the transverse force. The steel bearing plate also changed the transverse stress distribution in the concrete adjacent to the plate, but did not change the total transverse force.

Calculated transverse force during stage 2 was approximately 27 kip. When the embedded steel plate was present it attracted 3 kip, or approximately 10% of the force. This percentage is similar to stage 1. Presence of the steel plate changed the stress distribution in the concrete near the plate but it did not significantly affect the total transverse force at the end of the girder.

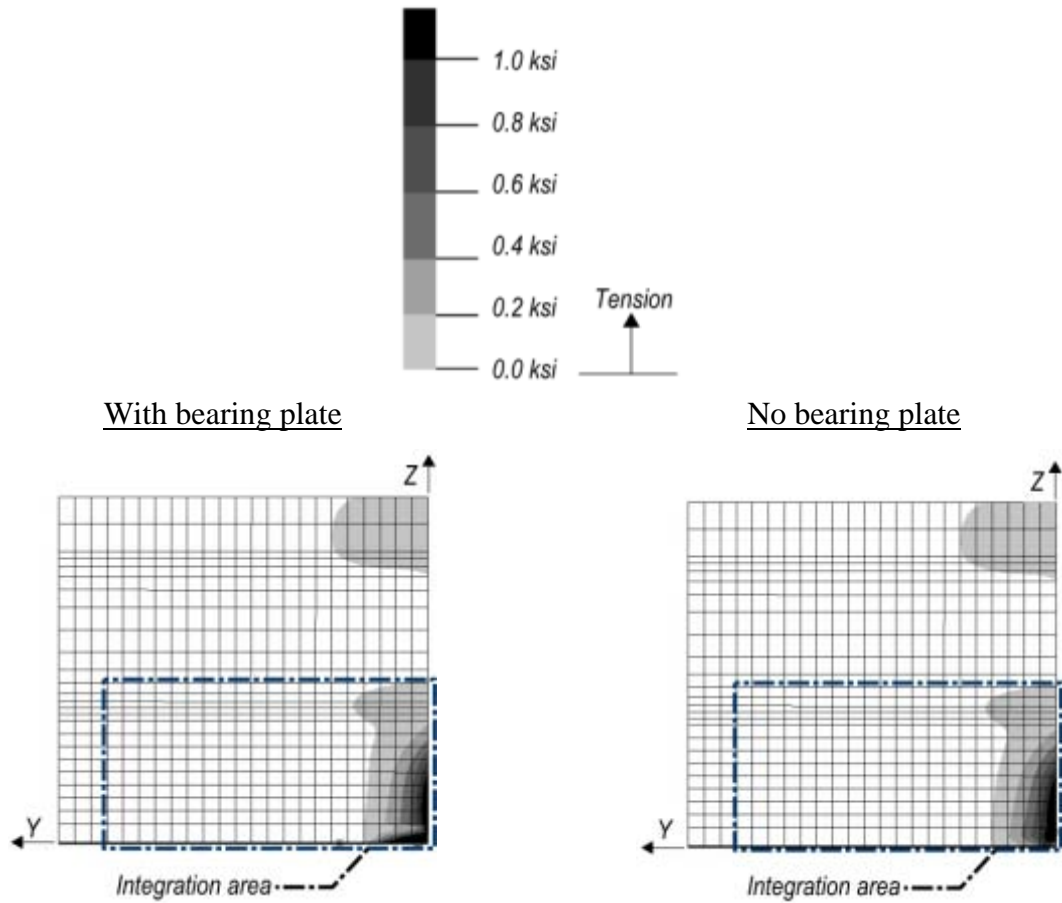


Figure 48–Transverse (x-x) stress distribution at stage 1 (outer strands cut) with bearing plate and without bearing plate

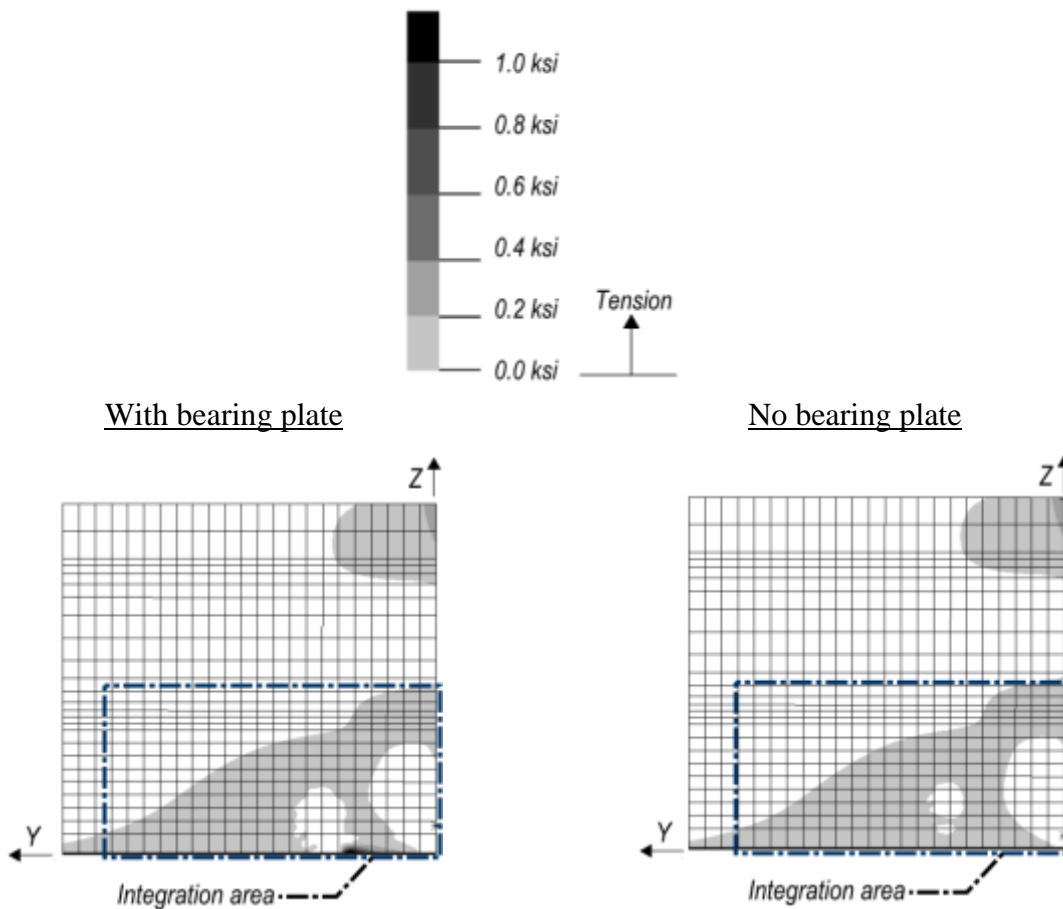


Figure 49–Transverse (x-x) stress distribution at stage 2 (all strands cut) with bearing plate and without bearing plate

Table 6–Bearing plate study summary of transverse (x-x) stresses and forces

	With bearing plate		No bearing plate	
	Max x-x stress at integration point (ksi)	Transverse tension force (kip)	Max x-x stress at integration point (ksi)	Transverse tension force (kip)
Outer strands cut (stage 1)	0.94	60.2 concrete 6.6 plate 66.8 total	1.16	66.9
All strands cut (stage 2)	0.15	24.9 concrete 3.0 plate 27.9 total	0.15	26.6

### 2.4.3 Transfer Length Parametric Study

This section presents results of a parametric study investigating the effect of transfer length on the magnitude of the transverse tensile force. FE models were created with transfer lengths that varied from 12.5 in. to 47.5 in. This range included lengths shorter than were observed in the experimental program as well as lengths longer than calculated using the AASHTO LRFD code.

The FIB model without a steel bearing plate was used in this study. Models considered the stage shown in Figure 46 when 50% of the strands were cut. This stage was selected because it corresponded to the largest transverse tensile forces.

The previously described integration procedure was used to calculate transverse tensile forces at the cross-section centerline. Transverse force at the centerline had an approximately linear relationship with the transfer length (Figure 50). The largest force corresponded to the shortest transfer length. Transverse tensile force decreased as the transfer length is increased. Thus, physical girders with relatively short transfer lengths have greater transverse forces and stresses than girders with longer transfer lengths.

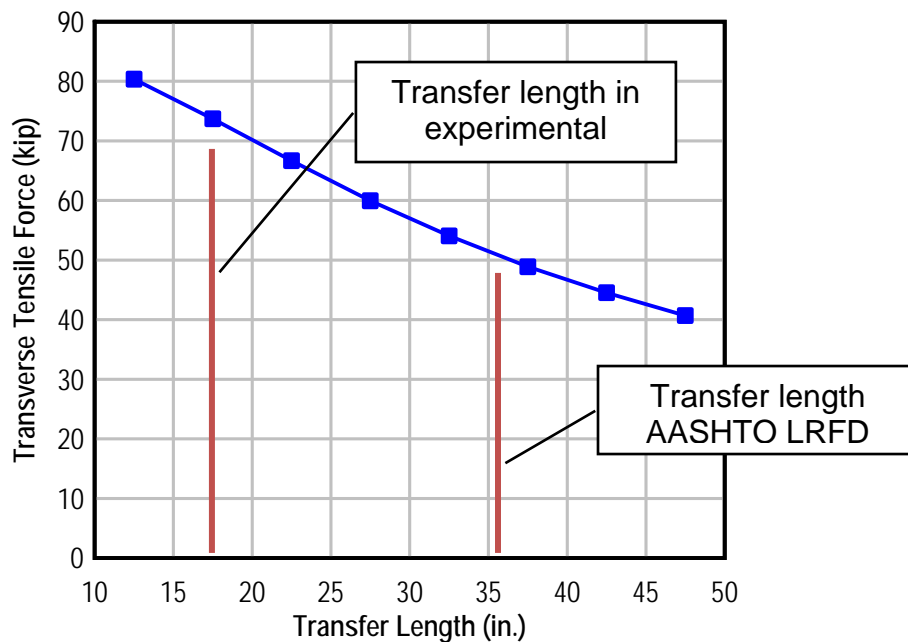


Figure 50–Transverse force vs. length of prestress transfer

According to the data in Figure 50, a 50% reduction in transfer length affected a 50% increase in transverse tensile force. For example, reducing the transfer length 50% from 40 in. to 20 in. resulted in an approximately 50% increase of transverse force from 48 kip to 70 kip.

Transverse tensile stresses due to prestressing forces are shown in Figure 53 and Figure 51 for sections through the centerline (CL) and bottom flange (MID). Tensile stresses formed near the member ends regardless of transfer length. The y-dimension of the tensile stress area was linearly related to the transfer length used in the FE models (Figure 53). Phase 1 experimental girders had a transfer length near 18in. For this transfer length, the FE model calculated that transverse tensile stress at the MID section of the bottom flange had a y-dimension of approximately 11in.

Transverse stress at the MID section is plotted as a function of y-coordinate in Figure 54 for transfer lengths of 17.5 in. and 42.5in. Stresses shown in the figure are from the condition when 30% of the strands had been cut. This condition produces the largest stresses on the MID section, and is a different condition that shown in Figure 51 and Figure 52. Figure 51 and Figure 52 show stresses for the stage when 50% of the strands have been cut. Shapes of the stress distributions in Figure 54 were representative of other bottom flange locations when only the strands outboard of the given location have been cut. For this condition, transverse tensile stresses were largest near the member end and were distributed in an approximately triangular shape. Also, tensile stresses for this condition were spread over a length of approximately 10 in. from the member end.

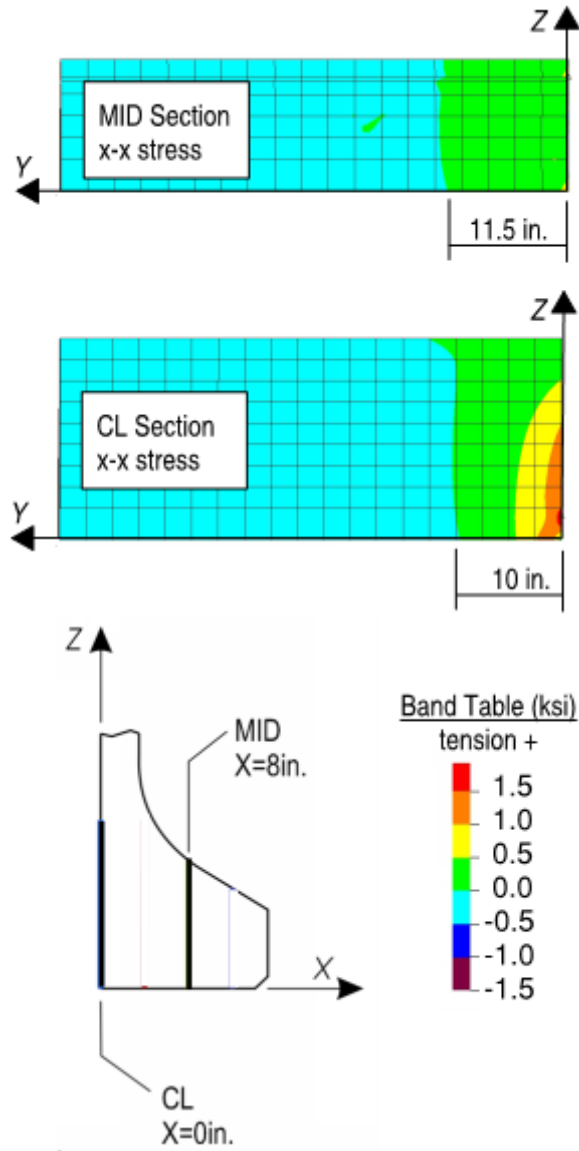


Figure 51–Transverse stress distribution with 17.5-in. transfer length (50% of strands cut)

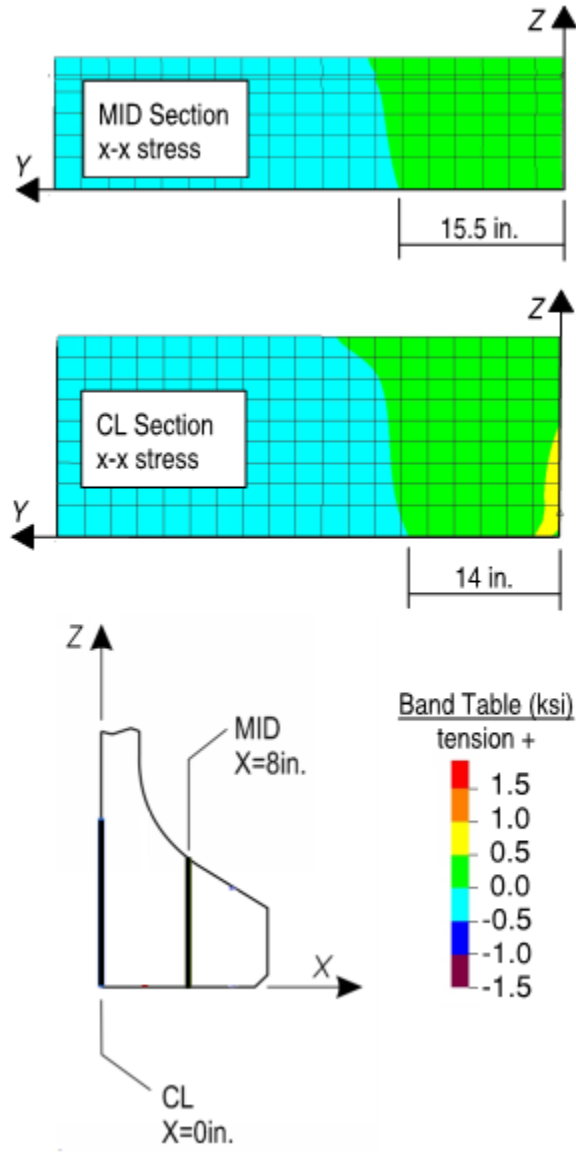


Figure 52–Transverse stress distribution with 42.5-in. transfer length (50% of strands cut)

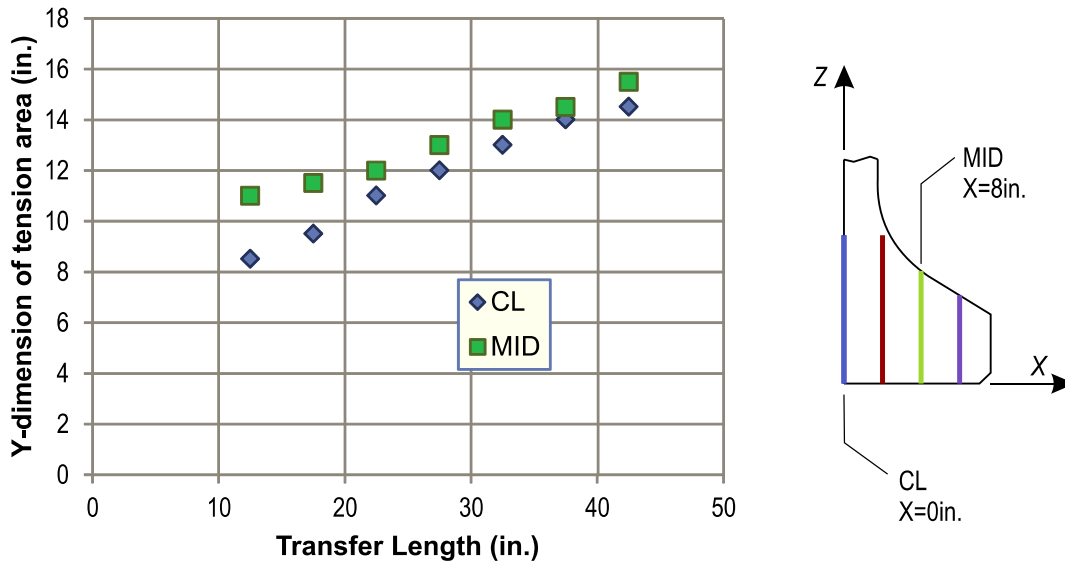


Figure 53–Length of tension area vs. transfer length (50% of strands cut)

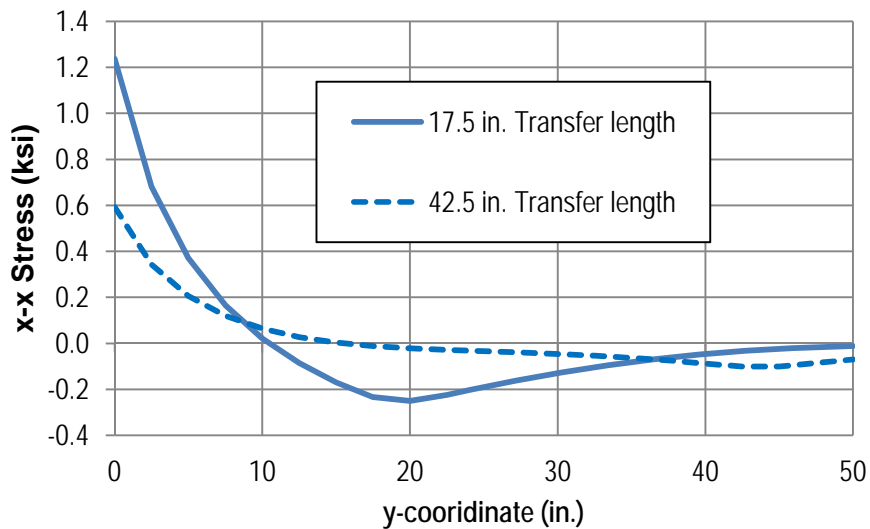


Figure 54–Transverse (x-x) stress at MID section through bottom flange (30% of strands cut)

#### 2.4.4 End Stresses due to Prestress Forces

Analytical results have shown that the largest stresses from the prestressing force occur at the girder end surface (Figure 46). In the experimental program, flange splitting cracks were often observed at the end surface (Figure 55). This section presents a study of stresses at the end surface due to prestressing forces. Results from this study will later be used in development of a model for serviceability design of bottom flanges.

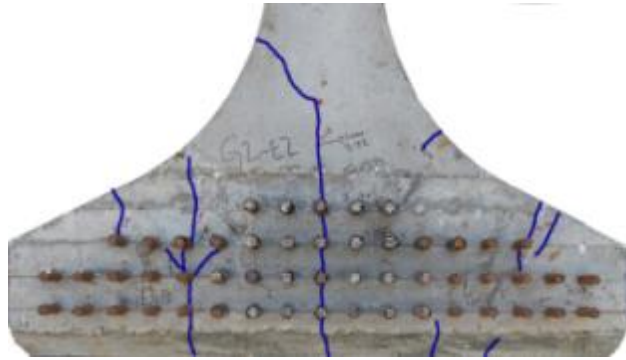


Figure 55–Flange splitting cracks at girder end

The FIB model without a steel bearing plate was used to study end stresses. Self-weight was eliminated to isolate the effects of the prestressing force on the section. A transfer length of 17.5 in. was used in the models. This length was chosen because previous results demonstrated that short transfer lengths produced the largest transverse effects. The refined mesh (Figure 38) was used in this study because stresses near the prestress forces (strands) were used in results interpretation. Strand pattern and strand cutting sequence demonstrated in Figure 46 was used in this study. This strand layout and cut pattern matched girders H, V, and D from the experimental program.

Four lines at the end surface of the model were selected for evaluation (Figure 56). Lines were selected based on the location of cracks observed in the test girders (Figure 55) and to give a representative analysis of the entire bottom flange end. A height of 15in. was used for the centerline (CL) and the web line (WEB) based on the height of flange splitting cracks in test girders. Height of the mid-flange (MID) and flange edge (EDGE) lines were limited by the flange height at those locations.

Transverse (x-x) stresses were considered along each line. This was done because tension stresses at the end of the bottom flange primarily acted in the x-direction. This was evident from the vertical orientation of cracks in the experimental girders (Figure 55). It was also observed in comparisons of transverse (x-x) and principal tension stresses at the end of the FE model (Figure 57). Transverse and principal tension stresses were effectively the same at areas away from the prestressing forces.

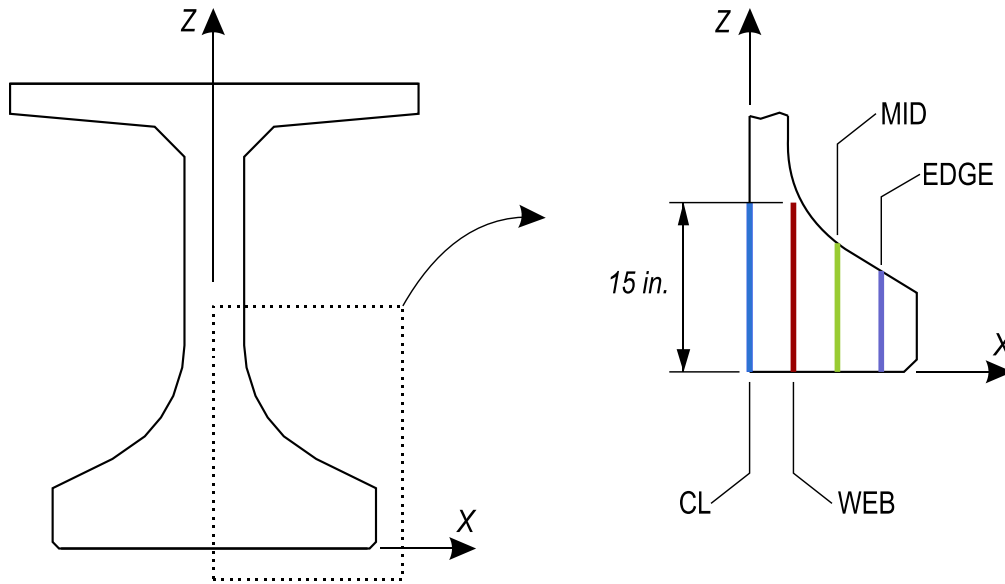


Figure 56—Lines for stress calculations

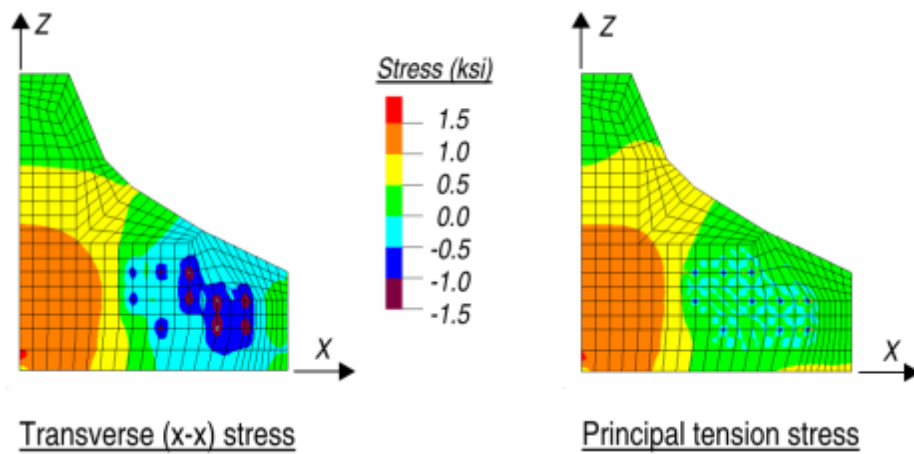


Figure 57—FE model stresses at girder end (50% strands cut)

Stresses along each line were calculated at each stage of prestress transfer using an outside-to-in strand cutting pattern. Stress concentrations occurred in the FE model at nodes where prestress forces were applied (Figure 57). In lieu of the concentrated stress values, stresses at these nodes were taken as the average stress from the adjacent nodes. This resulted in stress distributions such as that shown in Figure 58. Figure 58 shows the stress distribution at the mid-flange line for the stage when 50% of the strands had been cut. During this stage the two strands located on the mid-flange line were cut and resulted in compressive stresses near the strand locations.

The average stress along each line varied with the different stages of strand cutting as shown in Figure 59. The box markers on Figure 59 indicate the stage when strands on an individual line were cut. Average stress on a given line fell abruptly when strands along that line were cut. For example, average stress at the centerline went from 170 psi tension prior to cutting the centerline strands to 680 psi compression after the centerline strands were cut.

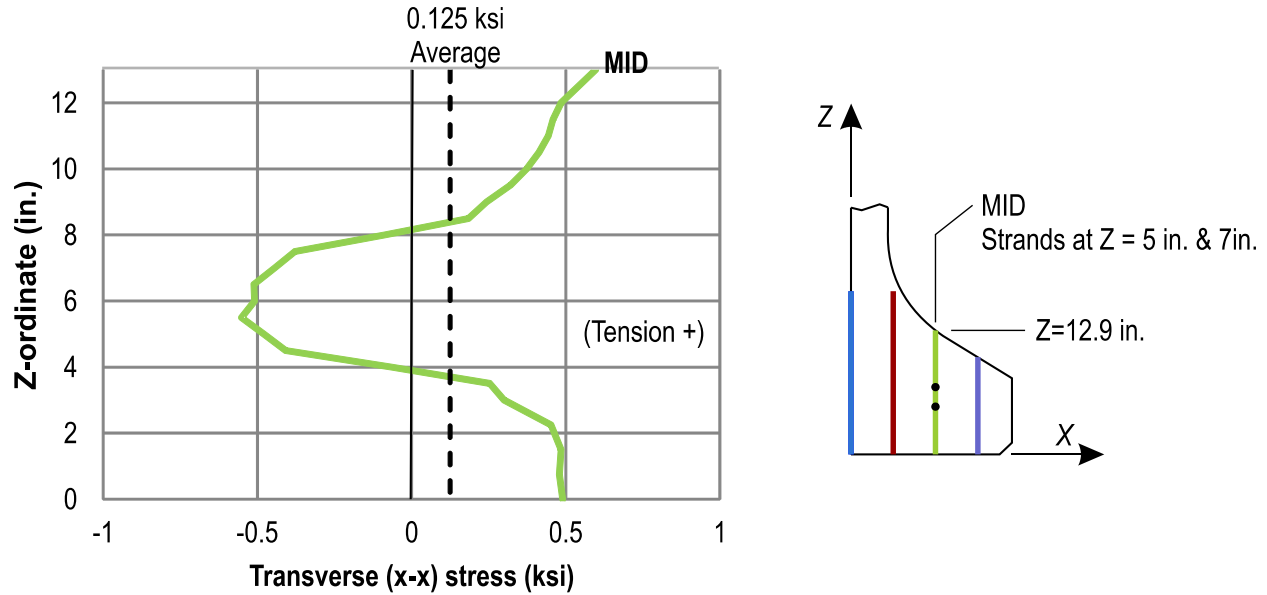


Figure 58–Transverse (x-x) stress at mid-flange line (50% strands cut)

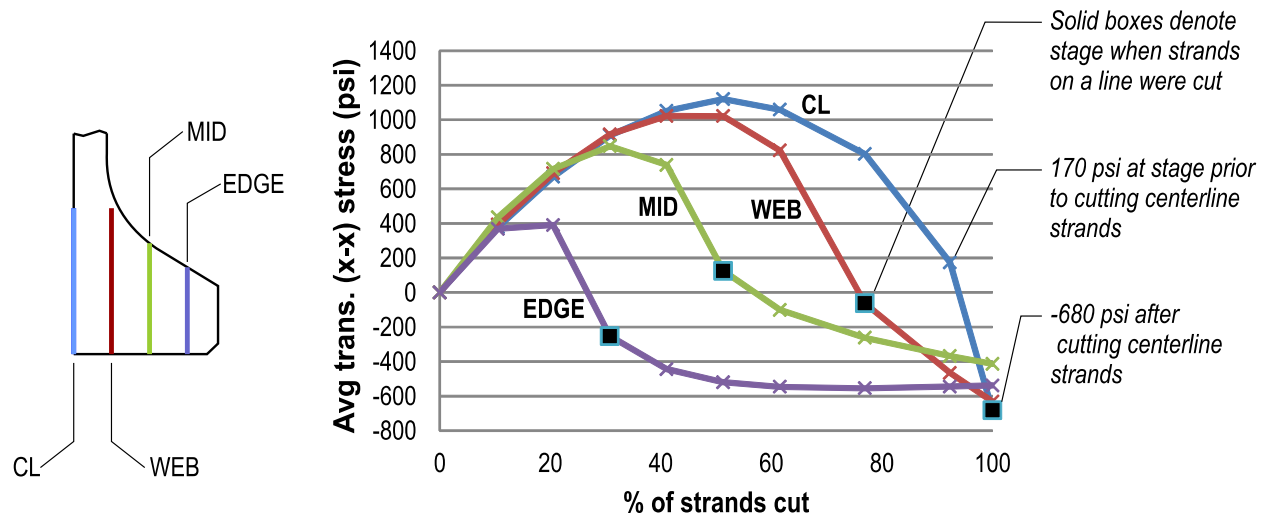


Figure 59–Average transverse (x-x) stress at end of girder due to strand cutting

Average stresses are summarized in Table 7 for each evaluation line. Tensile stress on a given line was greatest when only the strands outboard (closer to outside of flange) of the line

had been cut. Maximum tensile stresses ranged from 1.12 ksi to 0.39 ksi. The largest compressive stresses occurred after all strands had been cut. Maximum compressive stresses ranged from -0.68 ksi to -0.41 ksi. The average compressive stress after all strands had been cut was -0.57 ksi.

Table 7–Summary of transverse (x-x) stress at girder end due to strand cutting

Line	Maximum stress at any stage (ksi)	Stress at stage when strands on line were cut (ksi)	Stress after all strands were cut (ksi)
CL	1.12	-0.68	-0.68
WEB	1.02	-0.06	-0.63
MID	0.85	1.25	-0.41
EDGE	0.39	-0.25	-0.54
Average	0.85	-0.22	-0.57

#### 2.4.5 Transverse Force through Flange Sections

The models used in the previous section were utilized to calculate the transverse force acting on the MID and EDGE lines (Figure 56) through the bottom flange. These locations were of particular interest because of their proximity to flange splitting cracks observed in the experimental girders. The typical integration procedure was used to calculate the transverse tension force at these locations. Results are summarized in Table 8. The maximum transverse force at each location occurred when strands outboard of that location had been cut. Cutting of strands along each location reduced the transverse tension force by 45% at the MID line and 28% at the EDGE line.

Table 8–Summary of transverse (x-x) force at girder end due to strand cutting (FIB)

Section	Maximum force at any stage (kip)	Force at stage when strands on line were cut (kip)
MID	36.1	20.3
EDGE	15.8	11.3

The same procedure was used to investigate transverse tensile forces in the bottom flange of AASHTO Type IV girders. Strand pattern, element mesh, and analysis locations are shown in Figure 60 for the Type IV girder model. A transfer length of 18 in. was used for applying the prestressing forces. Strands were cut sequentially from outside-in. The transverse force on the

WEB and FLANGE lines were calculated at each stage of cutting. Results are listed in Table 9. For both locations, the maximum force occurred when only the strands outboard of the that location were cut. For example, the maximum force on the WEB section occurred when only the outermost six strands had been cut.

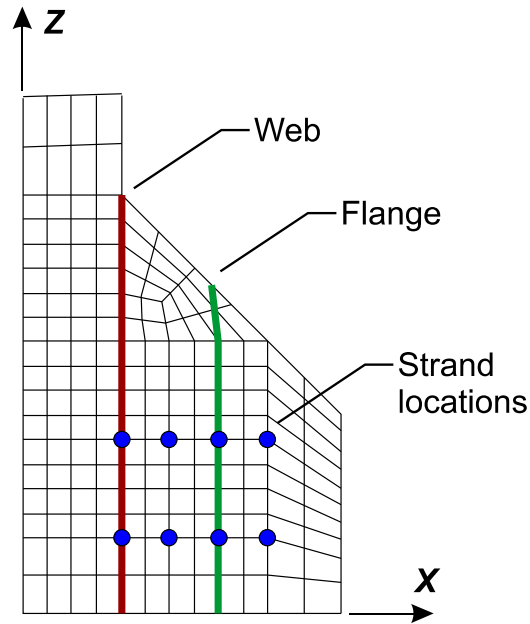


Figure 60–AASHTO Type IV FEA model and analysis lines

Table 9–Summary of transverse (x-x) force at girder end due to strand cutting (Type IV)

Section	Maximum force at any stage (kip)	Force at stage when strands on line were cut (kip)
WEB	11.4	7.0
FLANGE	5.9	5

As with the FIB model (Figure 54), tensile stresses in the Type IV model at the maximum stress condition are also distributed over a length of approximately 10in. from the member end. This is demonstrated by the stress distributions shown in Figure 61. Maximum stress for the WEB condition occurs when the outer six strands have been cut. Maximum stress at the FLANGE section occurs when the outer two strands have been cut. The maximum stress conditions are reported in the figure.

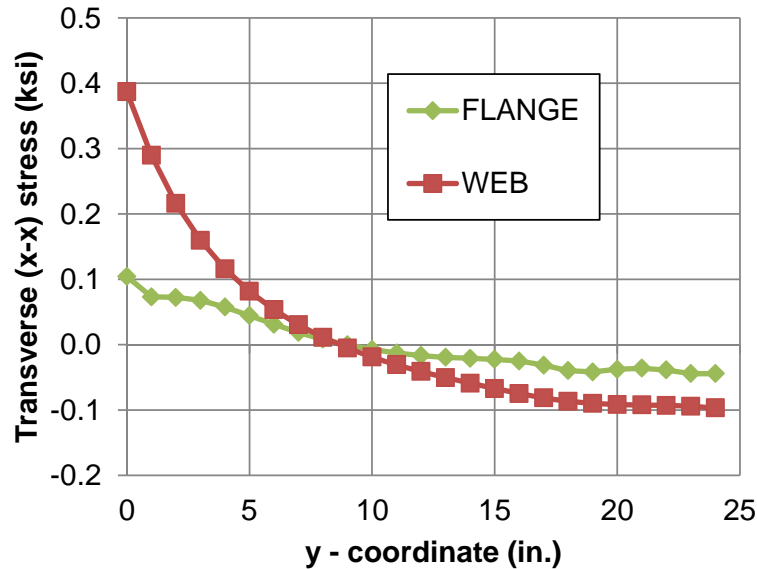


Figure 61–Transverse stress distribution in Type IV girder (maximum condition)

#### 2.4.6 Transverse Action due to Self-Weight

The test girders cambered upward during prestress transfer after the girder self-weight was overcome by the prestressing moment. In this condition the girders were supported vertically at the bottom edge at each end (Figure 34). The FIB FE model was used to evaluate the transverse stresses and forces that occurred due to the self-weight during this condition. Prestress loads in the model were removed leaving only the mass-proportional load which modeled the girder self-weight. Boundary conditions remained the same as previous models in this chapter. Because prestress loads were removed and self-weight remained, the displaced shape of the model was sagging rather than cambering.

Figure 62 shows the transverse (x-x) stresses at the centerline and end due to self-weight. Transverse tensile stresses were largest at the bottom of the girder near the end. Magnitudes of transverse stress due to self-weight were small relative to transverse stress due to prestressing as calculated in the previous section. This is in-part because the self-weight model was based on test girders H and V which were only approximately 35% as long as typical production girders with the same cross-section. Thus the self-weight stresses reported in Figure 62 were also only 35% of stresses in typical production girders.

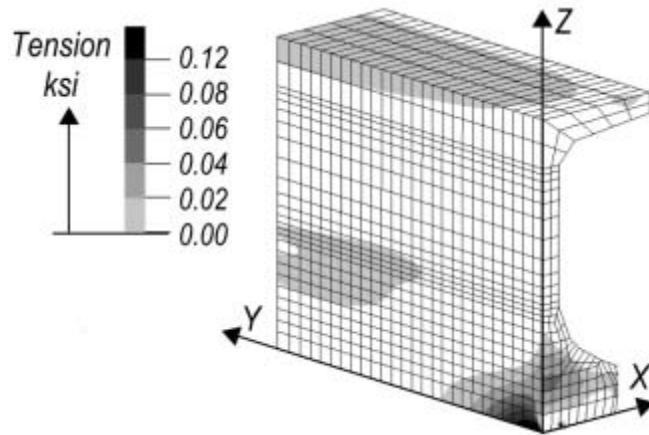


Figure 62–Transverse (x-x) stress due to self-weight

The typical integration procedure was used to calculate a transverse force of 6.7kip at the centerline. Self-weight reaction in the half-symmetry FE model was 12.0 kip. This reaction corresponded to a full reaction of 24 kip in the physical test girders. Thus the transverse force was equal to 28% of the physical reaction. This result is similar to the relationship derived between reaction force and transverse force shown in Figure 33.

Transverse stresses at the girder end were calculated at the same four lines (Figure 56) that were previously used to evaluate the effects of prestressing forces. Figure 63 shows stress that occurred at each line. Stresses below  $Z=2\text{in.}$  are not shown because numerical errors occurred in the FE model near the boundary condition.

Maximum and average stresses at each line are summarized in Table 10. Average stresses in the table conservatively ignored compressive stresses below  $Z=2\text{in.}$  The maximum tension stress was greatest at the centerline and was 3.4 times larger than at the line through the flange edge. The centerline section also had the largest average tension stress. At lines through the outer flange (MID and EDGE) the average stress was negligible or compressive. Average stresses at lines through the inner portion of the flange (CL and WEB) were tensile. Average tensile stresses at the CL and WEB lines were related to the reaction force by a factor of 1000. For example, the reaction force in the physical girders was 26 kip and the average tensile force on the inner lines was approximately 26 psi.

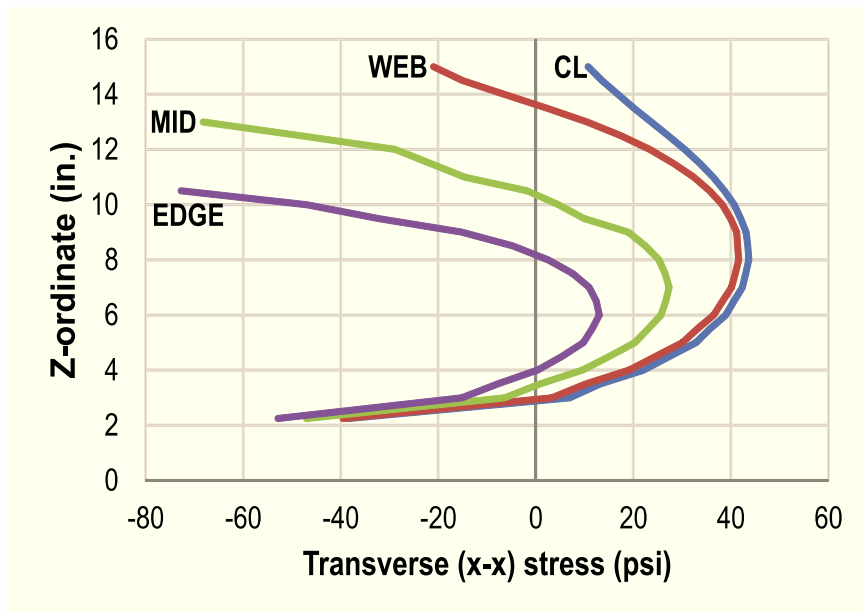
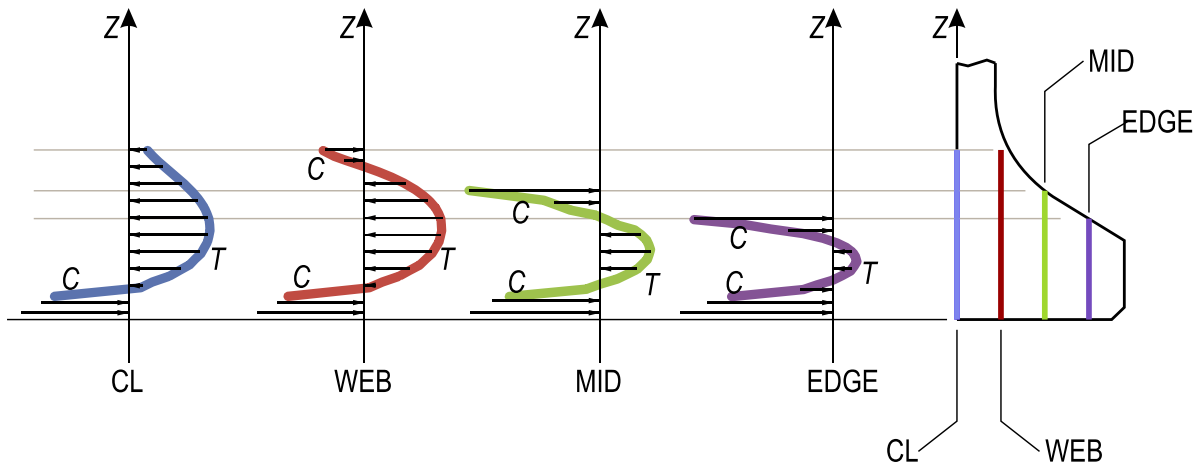


Figure 63–Transverse (x-x) stress due to self-weight

Table 10–Transverse (x-x) stress due to self-weight

	CL	WEB	MID	END
Maximum tension (psi)	44	42	27	13
Average stress (psi)	28	21	0.9	-10 (comp.)

## 2.5 Summary and Conclusions

Linear-elastic finite element modeling was used to evaluate stresses and forces in the bottom flange of Florida I-girders during prestress transfer. Each stage of prestress transfer (strand cutting) was considered in the models. Stresses and forces due to girder self-weight were also evaluated. Stresses due to the Hoyer effect were not considered in this chapter. Thus the conclusions below were based only on the effects of the prestress force and girder self-weight. Conclusions assumed strand cutting from outside-to-inside. The following conclusions were made based on results of the evaluations:

- For the given release sequence, the largest transverse (x-x) tensile stresses during prestress transfer occurred at the centerline of a section at the girder end. Centerline tension stresses were greatest when only the strands in the outer portion of the flange have been cut. Cutting of inner strands reduced this transverse tension.
- Embedded steel bearing plates carried transverse tension during and after prestress transfer. In the linear-elastic range plates in FIB girders carried 10% of the tension force due to prestressing. The portion carried by the plates does not vary during different stages of strand cutting.
- Transverse stress and forces were inversely proportional to strand transfer length. Thus the greatest transverse effects occurred in girders with the shortest transfer lengths. A 50% reduction in transfer length affected an approximately 50% increase in transverse tension.
- During prestress transfer the maximum transverse tensile stress on an arbitrary vertical line through the bottom flange occurred when only the strands outboard (closer to edge) of the line have been cut. Cutting of strands along or inboard (closer to centerline) of a line relieved tensile stresses on that line.
- Transverse stresses at the end of the bottom flange were compressive after all strands have been cut. An average compressive stress of 570 psi was calculated by the finite element models for conditions in experimental girders H and V.
- Self-weight reaction produced transverse tension forces in the bottom flange above the bearing. For Florida I-beams, the transverse tension force due to self-weight equaled 28% of the reaction.